

High-Throughput Screening for Boride Superconductors

Shiya Chen, Zepeng Wu, Zhen Zhang, Shunqing Wu, Kai-Ming Ho, Vladimir Antropov, and Yang Sun*



Cite This: <https://doi.org/10.1021/acs.inorgchem.4c00159>



Read Online

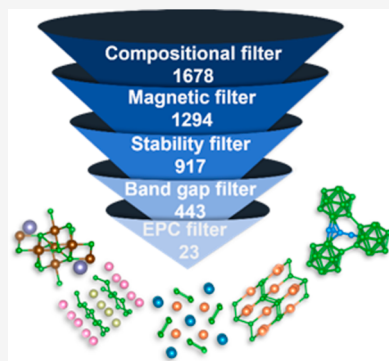
ACCESS |

Metrics & More

Article Recommendations

Supporting Information

ABSTRACT: A high-throughput screening using density functional calculations is performed to search for stable boride superconductors from the existing materials database. The workflow employs the fast frozen-phonon method as the descriptor to evaluate the superconducting properties quickly. Twenty-three stable candidates were identified during the screening. The superconductivity was obtained earlier experimentally or computationally for almost all found binary compounds. Previous studies on ternary borides are very limited. Our extensive search among ternary systems confirmed superconductivity in known systems and found several new compounds. Among these discovered superconducting ternary borides, TaMo₂B₂ shows the highest superconducting temperature of ~12 K. Most predicted compounds were synthesized previously; therefore, our predictions can be examined experimentally. Our work also demonstrates that the boride systems can have diverse structural motifs that lead to superconductivity.



1. INTRODUCTION

Superconducting materials have numerous applications in the modern society. The search for new superconductors with high critical superconducting temperature (T_c) is key to many future techniques in energy, medical care, transportation, and quantum computing. However, the conventional approaches to discovering new superconducting materials through direct experimental synthesis are time-consuming and resource-intensive. In recent years, it has been shown that computational prediction and design can greatly facilitate the discovery of new superconducting materials.^{1,2} The computational algorithms based on the density-functional perturbation theory (DFPT) can provide a satisfactory description of the electron-phonon coupling (EPC) and T_c for conventional superconductors. Due to the significant cost of the DFPT calculations, T_c calculations are now combined with information technologies such as data mining, machine learning, and high-throughput screening to guide the theoretical search of conventional superconductors.^{3–6}

The discovery of superconductivity in the structurally simple MgB₂ compound^{6,7} has stimulated substantial research efforts toward uncovering phonon-mediated superconductors within similar chemistries. Many attempts have been made to identify new superconducting phases derived from the MgB₂ compound, such as chemical doping or substitution, resulting in compounds like Mg_{1-x}Li_xB₂⁸ and Mg_{1-x}Zr_xB₂⁹, and MgB₂-like boride systems such as MoB₂¹⁰ and WB₂.¹¹ Recently, we have shown that the Brillouin zone-centered EPC strength can be a simple descriptor to identify phonon-mediated superconducting materials in hydrides and borides.^{12–17} This greatly reduced the computational cost in the high-throughput screening of boride superconductors. While we identified a few novel boride systems that exhibit an interesting high T_c ,

their thermodynamic stabilities are not sufficiently high for synthesis, and the structural motifs are still very close to MgB₂.¹³ Therefore, it remains unclear if other stable structural motifs in the borides can show feasible superconducting properties. In this study, we perform high-throughput screening on binary or ternary boride superconductors under ambient pressure from an existing materials database. These materials are stable and mostly synthesized before. We will use the zone-centered EPC strength as the main descriptor to identify their possible superconducting behavior. The structural motifs that can lead to possible T_c will be analyzed for the boride systems.

2. METHODS

Crystal structures were optimized by density functional theory (DFT) calculations, performed using the projector augmented wave (PAW) method¹⁸ within DFT as implemented in the VASP code.^{19,20} The exchange and correlation energy was treated with generalized gradient approximation (GGA) and parametrized by the Perdew–Burke–Ernzerhof (PBE) formula.²¹ A plane-wave basis was used with a kinetic energy cutoff of 520 eV, and the convergence criterion for the total energy was set to 10^{-5} eV. Monkhorst–Pack's sampling scheme²² was adopted for Brillouin zone sampling with a k -point grid of $2\pi \times 0.033 \text{ \AA}^{-1}$. The lattice vectors (supercell shape and size) and atomic coordinates were fully relaxed until the force on each atom was less than 0.01 eV/Å. The initial screening of the crystal structure

Received: January 12, 2024

Revised: April 8, 2024

Accepted: April 16, 2024

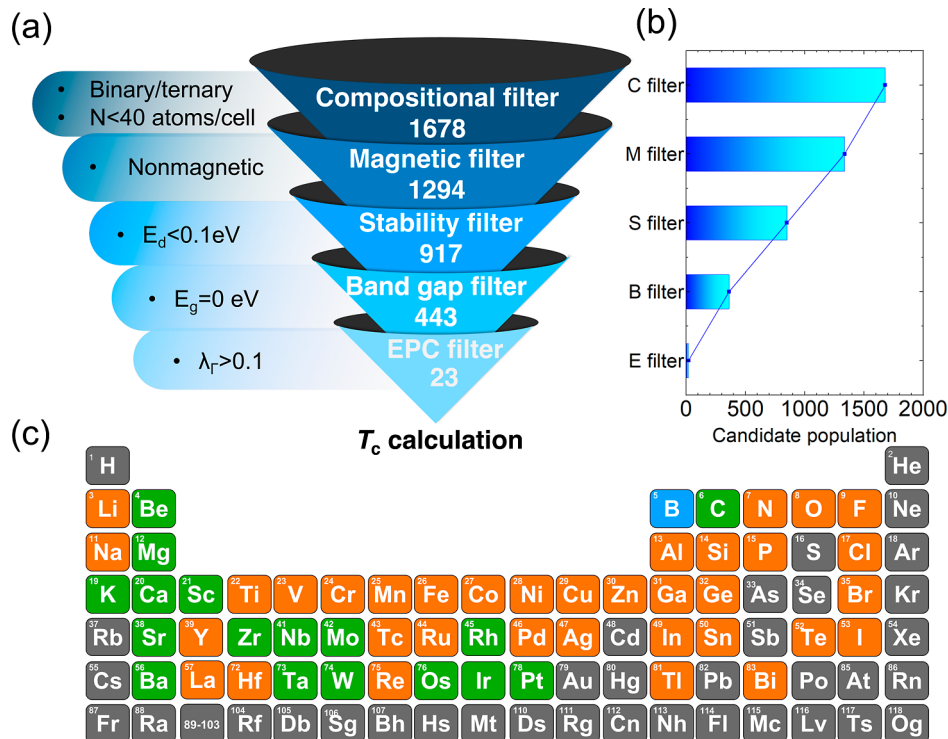


Figure 1. (a) Schematics of the screening workflow. (b) Bar chart of populations after each filter. (c) Elements involved in the screening. Orange indicates the elements in the initial pool after the B filter. Green indicates the remaining elements after the E filter.

was based on the MPRester package, which allows for the materials screening from the Materials Project database.²³

The high-throughput screening of strong EPC in these metal borides is based on the fast frozen-phonon calculation of the zone-center EPC strength¹² defined by

$$\lambda_\Gamma = \sum_v \lambda_{\Gamma v} \quad (1)$$

where \sum_v indicates the summation of all modes at zone-center Γ . $\lambda_{\Gamma v}$ is defined by

$$\lambda_{\Gamma v} = \frac{\tilde{\omega}_{\Gamma v}^2 - \omega_{\Gamma v}^2}{4\omega_{\Gamma v}^2} \quad (2)$$

where $\tilde{\omega}_{\Gamma v}$ and $\omega_{\Gamma v}$ are unscreened and screened phonon frequencies of mode v at the zone center, respectively. The screened phonon frequencies were calculated using the primitive cell and finite displacement methods implemented in the Phonopy code.²⁴ The displacement amplitude in the frozen-phonon calculations was 0.02 Å. The convergence criterion of the total energy was 10^{-8} eV.

The calculations of full Brillouin-zone EPC constants and the superconducting temperature T_c were performed based on DFPT²⁵ implemented in the Quantum ESPRESSO code.^{19,26,27} Ultrasoft pseudopotentials²⁸ with the PBE functional were used with a kinetic energy cutoff of 80 Ry and a charge density cutoff of 800 Ry. After the convergence test, the plane-wave cutoff and the charge density cutoff were chosen to be 80 and 640 Ry, respectively. The Monkhorst-Pack's sampling scheme²² was adopted for Brillouin-zone sampling with a k -point grid of $2\pi \times 0.025\text{ \AA}^{-1}$. Self-consistent field (SCF) calculations were performed with a dense k mesh of twice the scale of the sampling scheme, followed by the DFPT calculation with the k mesh of the same sampling scheme and setting the q mesh to half of the k mesh. We used 0.015 Ry as the Gaussian broadening for T_c calculation. The test on TaMo₂B₂ in Figure S18 suggests that the setting was sufficient to converge the T_c in 1–2 K.

The isotropic Eliashberg spectral function was obtained via the average over the Brillouin zone^{29,30}

$$\alpha^2(\omega)F(\omega) = \frac{1}{2N(\epsilon_F)} \sum_{qv} \frac{\gamma_{qv}}{\hbar\omega_{qv}} \delta(\omega - \omega_{qv}) \quad (3)$$

where $N(\epsilon_F)$ is the density of states at the Fermi level ϵ_F and ω_{qv} denotes the phonon frequency of mode v with wave vector q . γ_{qv} is the phonon line width defined by

$$\gamma_{qv} = \frac{2\pi\omega_{qv}}{\Omega_{BZ}} \sum_{ij} \int d^3k |g_{k,qv}^{ij}|^2 \delta(\epsilon_{q,i} - \epsilon_F) \delta(\epsilon_{k+q,j} - \epsilon_F) \quad (4)$$

where $g_{k,qv}^{ij}$ is the EPC matrix element and $\epsilon_{q,i}$ and $\epsilon_{k+q,j}$ are eigenvalues of Kohn–Sham orbitals at bands i, j , and wave vectors q, k . The full Brillouin zone EPC constant λ was determined through the integration of the Eliashberg spectral function

$$\lambda = 2 \int \frac{\alpha^2(\omega)F(\omega)}{\omega} d\omega \quad (5)$$

T_c is obtained with the analytical McMillan formula²⁹ modified by Allen–Dynes^{15,31}

$$T_c = \frac{\omega_{\log}}{1.2} \exp \left[\frac{-1.04(1 + \lambda)}{\lambda(1 - 0.62\mu^*) - \mu^*} \right] \quad (6)$$

where ω_{\log} is the logarithmic average frequency

$$\omega_{\log} = \exp \left[\frac{2}{\lambda} \int \frac{d\omega}{\omega} \alpha^2(\omega)F(\omega) \ln \omega \right] \quad (7)$$

and μ^* is the effectively screened Coulomb repulsion constant, set as 0.1 in our calculations.

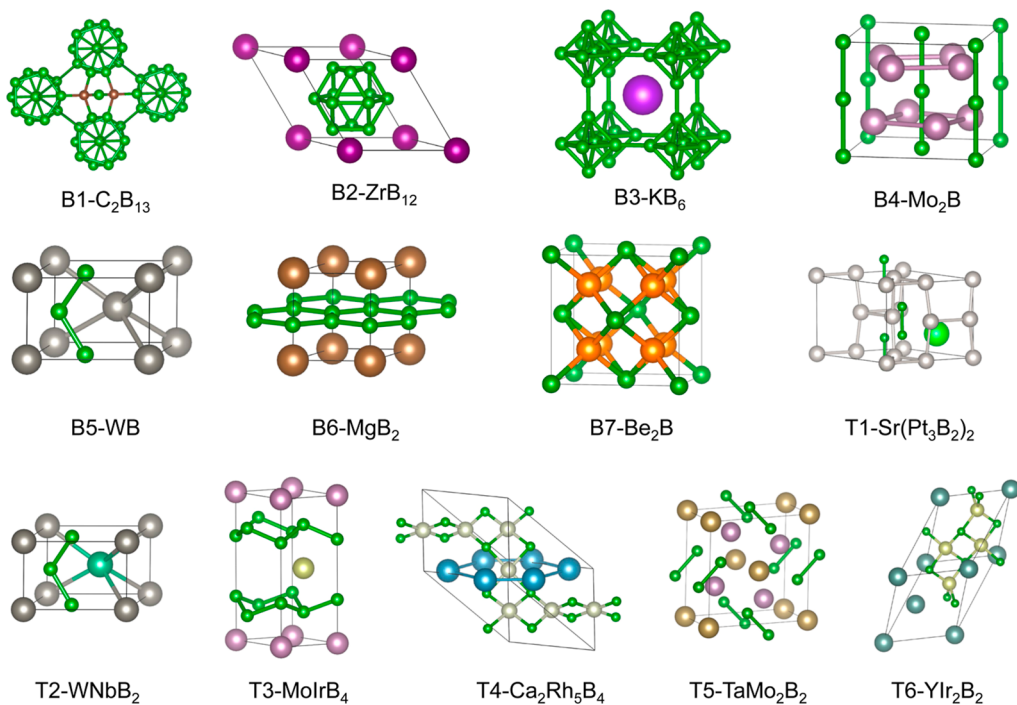
3. RESULTS AND DISCUSSION

3.1. High-Throughput Screening. Figure 1 summarizes the screening strategy for superconducting boride compounds.²³ We design five criteria to filter low-energy binary or ternary borides for promising superconducting materials from the structural database.³² These criteria include a

Table 1. Structural and Superconductivity Properties of the Screened Candidate^a

structural motif	compound	λ_{Γ}	λ_{BZ}	synthesized?	experimental T_c	calculated T_c	space group
B1	C_2B_{13}	0.36	0.81 ³⁵	Y ³⁶	N ³⁷	15–30 K ³⁵	$R\bar{3}m$
B2	ZrB_{12}	0.14	0.61	Y ³⁸	6.0 K ³⁹	6.9 K*	$Fm\bar{3}m$
B3	KB_6	0.13	0.56 ⁵	Y ⁴⁰	N ⁴¹	16.8 K ⁵	$Pm\bar{3}m$
B4	Mo_2B	0.27	0.94	Y ⁴²	6.0 K ⁴³	7.0 K*	$I4/mcm$
	Ta_2B	0.15		Y ⁴²	3 K ⁴⁴	-	
B5	WB	0.34	0.56	Y ⁴⁵	2.0 K ⁴⁵	5.3 K*	$Cmcm$
	MoB	0.32		Y ⁴⁵	2.4 K ⁴⁵		
B6	MgB_2	0.42	0.70 ⁷	Y ⁴⁹	39 K ⁶	22 K ⁷	$P6/mmm$
	TaB_2	0.12	0.73 ⁴⁶	Y ⁵⁰	9 K ⁵³	12 K ⁴⁶	
	NbB_2	0.10	0.71 ⁴⁷	Y ⁵¹	9 K ⁴⁵	5.7–19.4 K ⁴⁷	
	ScB_2	0.05	0.47 ⁴⁸	Y ⁵²	1.5 K ⁴⁸	1.62 K ⁴⁸	
B7	Be_2B	0.34	0.51 ⁵⁴	Y ⁵⁵	N ⁵⁶	~10 K ⁵⁴	$Fm\bar{3}m$
T1	$Sr(Pt_3B_2)_2$	0.82	1.59	Y ⁵⁷	2.7 K ⁵⁷	4.1 K*	$P\bar{3}m1$
	$Ba(Pt_3B_2)_2$	0.64		Y ⁵⁷	5 K ⁵⁷	-	
T2	$WNbB_2$	0.22	0.44	Y ⁵¹	?	2.4 K*	$Amm2$
	$TaMoB_2$	0.20	0.81	N	?	5 K*	
T3	$MoIrB_4$	0.10	0.48	N	?	4 K*	$P\bar{6}m2$
	$OsWB_4$	0.10		N	?	-	
T4	$Ca_2Rh_5B_4$	0.25	0.72	Y ⁵⁸	?	4.9 K*	$Fmmm$
	$Sr_2Rh_5B_4$	0.22		Y ⁵⁸	?	-	
T5	$TaMo_2B_2$	0.93	0.81	Y ⁵⁹	?	12 K*	$P4/mbm$
	$NbMo_2B_2$	0.57	0.76	Y ⁶⁰	?	-	
T6	YIr_2B_2	0.38	0.97	Y ⁶¹	3.3 K ⁶²	7.4 K*	$Fddd$

^a λ_{Γ} is from fast zone-center EPC calculations, while λ_{BZ} is EPC from the full Brillouin zone calculation. Star (*) indicates the calculated result from this work. "Y" indicates that the compound was previously synthesized according to the Inorganic Crystal Structure Database (ICSD).³⁴ "N" indicates that the compound was not synthesized or non-superconducting in experiments. "?" indicates the lack of experimental investigation on superconductivity. "-" indicates that T_c was not calculated theoretically.

**Figure 2. Structural motifs of potential superconducting boride phases.**

chemical composition filter (C), a magnetic filter (M), a stability filter (S), a band gap filter (B), and an EPC strength filter (E). These filters are defined as follows.

The C filter selects binary or ternary boride compounds containing fewer than 40 atoms in the primitive cell. These compounds contain various elements, as shown in Figure 1b.

We eliminated compounds with 4f and 5f elements except for La due to the problematic DFT calculation for f electrons. The primary goal is to pinpoint simple binary or ternary borides for further consideration. This step effectively narrows down the candidate pool, resulting in 1678 phases for further evaluation.

The M filter removes compounds with finite magnetic moment (larger than $0.01 \mu_B/\text{atom}$) from the pool because the superconducting and magnetic phases are mutually exclusive.

The S filter attempts to select stable or low-energy metastable phases that exist in experiments or have a large chance of being synthesized. We employ the energy above the convex hull (E_d) less than $0.1 \text{ eV}/\text{atom}$ as the criterion. E_d measures the energy of a material to decompose into a set of more stable compounds. Larger E_d indicates poorer stability, while a zero E_d indicates the most stable phase. $0.1 \text{ eV}/\text{atom}$ corresponds to the energy of thermal fluctuation $\sim 1100 \text{ K}$, a typical energy scale for the boride phase that can be synthesized experimentally.¹⁵ The filter removed 377 unstable phases from the pool.

The B filter selects metallic materials with zero band gap, a characteristic commonly associated with superconductors. By implementing this filter, we eliminate semiconductors or insulators that, due to their electronic structure, are unlikely to exhibit superconducting behavior.

By applying these filters and quantifying the number of materials at each step, we ensure that the selected compounds align with our design principle for potential superconductivity. Figure 1a shows the screening results in 443 candidates after the B filter. Before the final T_c calculations, we apply the E filter to identify structures with strong EPC strength based on the fast frozen-phonon calculations of zone-center EPC strength.¹² This method is particularly efficient in identifying phonon-mediated superconductors in the borides and hydrides, where the zone-center phonon modes contributed significantly to the EPC.^{13,15,16,33} By setting a threshold of 0.1 for the zone-center EPC strength ($\lambda_\Gamma > 0.1$), we ultimately identified 23 materials for further superconductivity calculations. The zone-center EPC contributions are shown in Figures S1–S11. Comparing the candidate population after each filter in Figure 1b, it is evident that the EPC screening reduced the most significant fraction (95%) of the parent structure pool, suggesting strong EPC as a rare property in the materials.

The classified 23 candidates contain 12 binary compounds and 11 ternary compounds. As shown in Figure 1c, the elements involved in these compounds before the E filter are evenly distributed in the elemental table and do not show a chemical preference. After applying the EPC filter, the remaining elements are mostly on the left side of the elemental table, showing a preference for group-II elements. Based on the atomic packing, we classify the structures into 7 families for binary compounds and 6 for ternary compounds. The structural information and motifs are shown in Table 1 and Figure 2, respectively. The boron atoms exhibit diverse atomic packing in these motifs. In Motif B1, B2, and B3, boron atoms pack as B_{13} , B_{12} , and B_6 polyhedra, respectively. In Motif B4 and B5, boron atoms pack as a chain. In Motif B6, boron forms a hexagonal layer. In Motif B7, boron forms a 3D structure with the metal atom. In ternary phases, boron's packing shows a similar motif as the ones in binary phases. In Motif T1, two boron atoms form a dumbbell structure. Motif T2 is essentially the same as Motif B5 except that different metal elements occupy the metal site. Motif T3 is like B6, while the hexagonal boron layer is buckled. In Motif T4, boron and small metal atoms (Rh in the figure) form a square ring. Motif T5 also has a B_2 dumbbell like the one in T1. In Motif T6, each Ir atom is connected to four surrounding B atoms to form a ring similar to the one in B7.

The screened superconducting phase shows diverse chemical and structural characteristics. The following sections review relevant literature for synthesized superconductors in these structures. We will select a specific compound to conduct full Brillouin zone EPC and T_c calculations for structures that have not been explored. These will validate the reliability of our screening methodology and potentially discover new superconducting materials that have not been previously documented.

3.2. Binary Borides. Comparing with the literature, we find that most current binary candidates possess phonon-mediated superconductivity, as shown in Table 1. Except for MgB_2 , other compounds in the experimental study show T_c lower than 10 K .

ZrB_{12} is a two-gap strongly coupled superconductor with an experimental T_c of $\sim 6 \text{ K}$.^{39,63} In our calculation, the T_c of ZrB_{12} was estimated at 6.92 K by the McMillan–Allen–Dynes (MAD) formula with $\lambda = 0.61$. The low-frequency phonon modes dominated by the Zr atom contribute 0.34 to λ , as shown in Figure S12.

Kayhan reported a low T_c of $\sim 2 \text{ K}$ in WB and MoB compounds. The B6 structure is from the MgB_2 family, frequently studied.^{6,45–53}

Mo_2B was recently reported as a weakly coupled superconductor with a T_c of $\sim 6 \text{ K}$.⁴³ However, some imaginary phonon modes exist at the Γ point, as shown in Figure S13. It should be noted that the appearance of imaginary frequency modes in the phonon spectrum does not necessarily imply realistic instability. It was suggested that the lack of consideration of anharmonic effects may cause computational instability of $I4/mcm$ Mo_2B .⁶⁴ The anharmonic effect can stabilize structures, as seen in CaSiO_3 ,⁶⁵ SrTiO_3 ,⁶⁷ and Na_2TiSb .⁶⁸ Other effects, such as temperature, charge density wave, vacancies, and structural distortions, can also stabilize the structure. It was suggested that the dynamically stable $I4/m$ phase could better explain the Mo_2B structure at the harmonic level.⁶⁹ However, the structure of the $I4/m$ phase is very similar to the $I4/mcm$ phase, and their XRD data were indistinguishable.

Some predicted superconductors, such as C_2B_{13} , KB_6 , and Be_2B , were not demonstrated by the experiment. The structure of C_2B_{13} was similar to B_4C , where the B icosahedra were connected by B/C atoms. The C_2B_{13} structure was predicted to be a potential superconductor with a T_c of $15–30 \text{ K}$.³⁵ However, the experimentally synthesized C_2B_{13} contains a large number of defects, leading to a semiconducting state that hinders its superconductivity.³⁷

KB_6 was calculated with a T_c of 16.8 K .⁴⁰ However, KB_6 has not yet exhibited superconductivity in experiments. Possible factors include small, mutually insulated grains, inhibitory oxide impurities, adverse electronic localization, low magnetization experiment temperatures, and a disparity between theoretical predictions and practical superconductivity.⁴¹ Be_2B was also predicted to be a potential superconductor⁷⁰ with a T_c of $\sim 10 \text{ K}$.⁵⁴ Unfortunately, the experimentally synthesized Be_2B contained significant defects that induced uncertainties on its stoichiometry.⁵⁶

3.3. Ternary Borides. Table 1 shows several ternary borides as potential superconductors with $\lambda_\Gamma > 0.1$. Notably, among these ternary borides, the T1 family comprising $\text{Sr}(\text{Pt}_3\text{B}_2)_2$ and $\text{Ba}(\text{Pt}_3\text{B}_2)_2$ and T6 family (YIr_2B_2) were confirmed as superconductors by the experiment.^{57,62,71} The experimentally synthesized Sr–Pt–B phase shows a partial

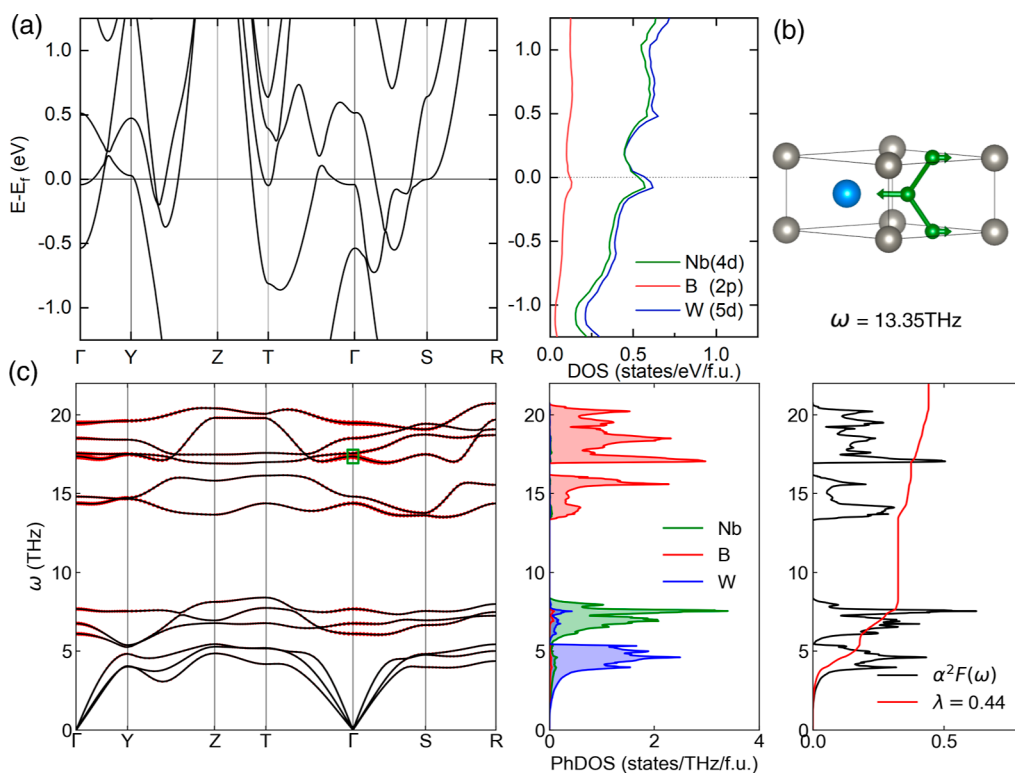


Figure 3. (a) Band structure and projected density of states of WNbB₂. (b) Structure of WNbB₂. The arrow represents the eigenvector of the phonon mode at the Γ point with a frequency of 13.35 THz, noted in (c). Blue is W, gray is Nb, and green is B. (c) Phonon spectrum, projected phonon density of state, and the Eliashberg spectral function of WNbB₂. The red bands on the phonon spectrum indicate the phonon line width.

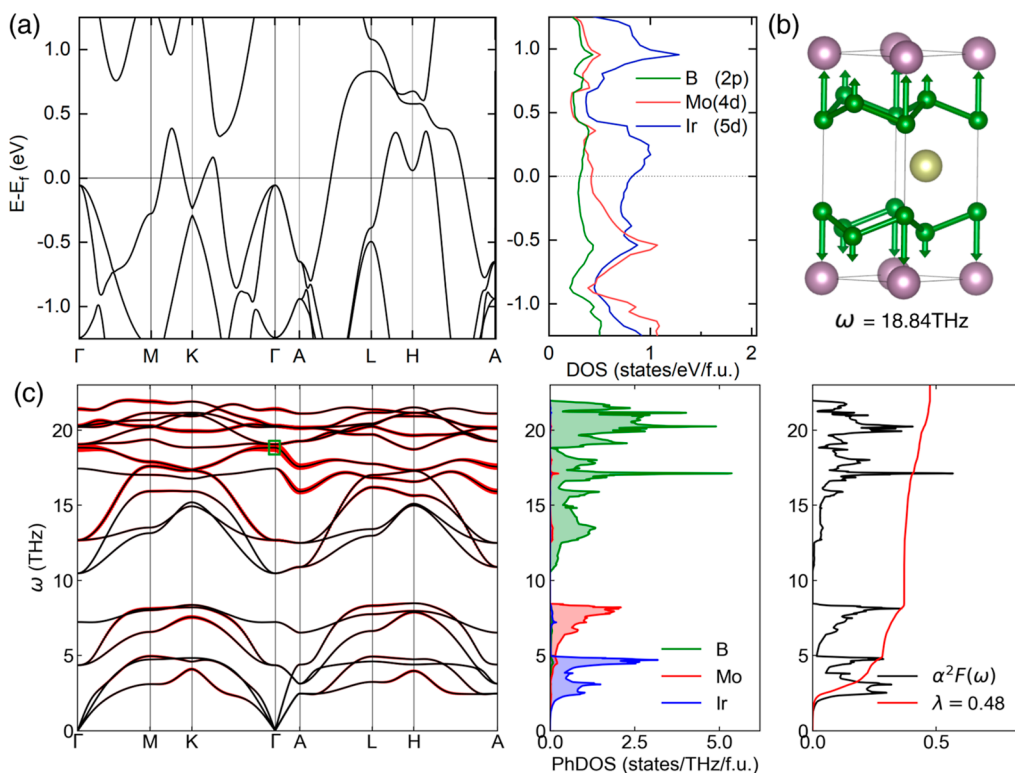


Figure 4. (a) Band structure and projected density of states of MoIrB₄. (b) Structure of MoIrB₄. The arrow represents the eigenvector of the phonon mode at the Γ point with a frequency of 18.84 THz, noted in (c). Purple is Mo, yellow is Ir, and green is B. (c) Phonon spectrum, projected phonon density of state, and the Eliashberg spectral function of MoIrB₄. The red bands on the phonon spectrum indicate the phonon line width.

occupancy on Sr sites, resulting in a Sr_{0.66}Pt₃B₂ composition.⁵⁷ In our calculation, we used the same structure but with a

vacancy and a fully occupied Sr site to study this compound, as shown in Figure S15. This may lead to the imaginary phonon

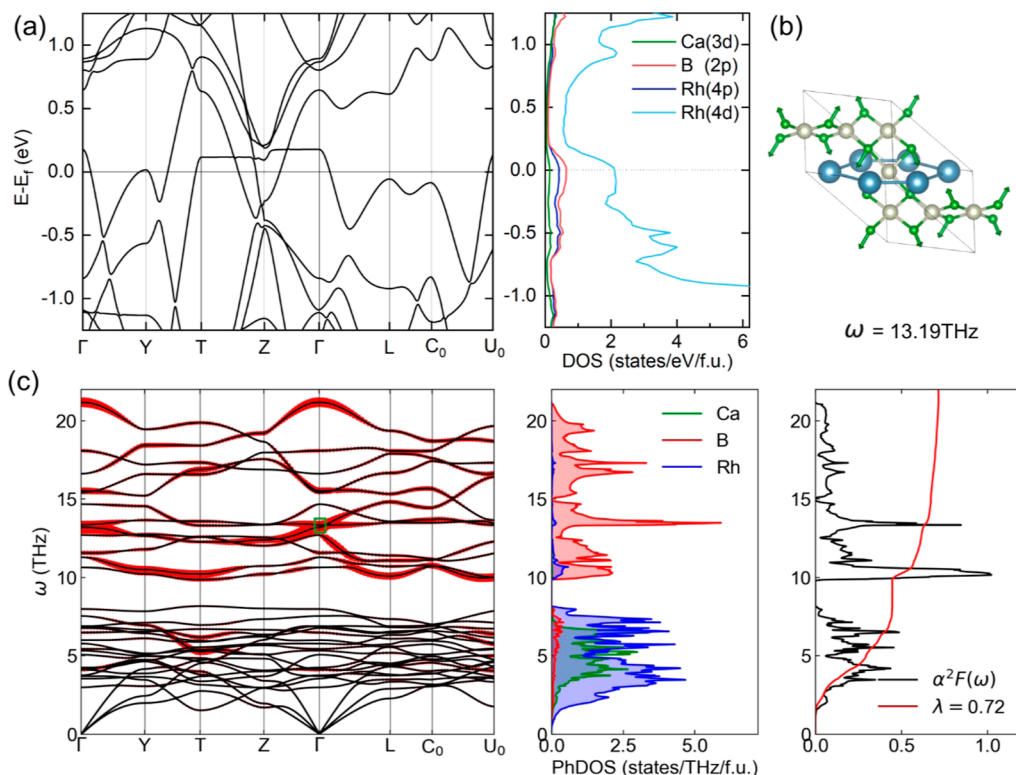


Figure 5. (a) Band structure and projected density of states of $\text{Ca}_2\text{Rh}_5\text{B}_4$. (b) Structure of $\text{Ca}_2\text{Rh}_5\text{B}_4$. The arrow represents the eigenvector of the phonon mode at the Γ point with a frequency of 13.19 THz, noted in (c). Blue is Ca, yellow is Rh, and green is B. (c) Phonon spectrum, projected phonon density of state, and the Eliashberg spectrum of $\text{Ca}_2\text{Rh}_5\text{B}_4$. The red bands on the phonon spectrum indicate the strength of EPC.

modes shown in Figure S15c. Because the T_c calculations with correct treatment of dynamical instability and partially occupied structure are expensive, we made a rough estimation of T_c for $\text{Sr}(\text{Pt}_3\text{B}_2)_2$ under the assumption that the imaginary phonon modes do not contribute to the EPC, as did in previous high-throughput works.⁷² It shows that the approximated structure has a similar T_c (4.1 K) compared to the experimental data (2.7 K). The full Brillouin-zone EPC calculation results of YIr_2B_2 are shown in Figure S16. Other ternary families have not been investigated for superconductivity by the experiment or theory. We select one compound for each family in T2–T5 to perform DFPT calculations. The calculated full Brillouin-zone EPC constant and estimated T_c with the MAD formula are shown in Table 1 and discussed below.

3.3.1. WNbB_2 . WNbB_2 shares a similar structure to the orthorhombic WB (space group $Cmcm$). The B atoms in WNbB_2 exist as a one-dimensional B-atom chain, see Figure 3b. As in Figure 3a, a van Hove singularity is near the Fermi level, mainly dominated by the Nb 4d orbital and W 5d orbital. On the other hand, due to the significant mass differences between B and Nb/W, the phonon modes are entirely decoupled. Nb and W contribute to the EPC of low phonon frequency modes, while B contributes to the EPC of high phonon frequency modes. Figure 3b shows the phonon mode with a frequency of 13.35 THz at the Γ point, which possesses a large phonon line width, contributing major EPC strength in high-frequency phonons. The T_c of WNbB_2 is ~2 K, smaller than WB (5.3 K). The main reason for the difference in T_c between WNbB_2 and WB is that the EPC contributed by low-frequency phonons in WB is higher than in WNbB_2 . Compared with WB, introducing the Nb element in WNbB_2

increases the frequency of some low-frequency optical phonons, suppresses the softening of phonons, and weakens EPC.

3.3.2. MoIrB_4 . The band structure and phonon spectrum of MoIrB_4 are shown in Figure 4. The projected electron density of states indicates that the Ir-5d orbital dominates the $N(E_F)$, and Ir contributes significantly to EPC. The calculated T_c of MoIrB_4 is 4 K. MoIrB_4 has a ReB₂-type structure and exhibits layered characteristics. It shows some analogy to MgB₂, in which the B atoms form interlayer hexagonal rings between metal layers. The distinction between MoIrB_4 and MgB₂ lies in the fact that the B hexagonal rings in MoIrB_4 are not coplanar but adopt a buckled three-dimensional conformation. This buckled structure may originate from the metal atoms above the B rings instead of at the ring centers, which compress the B rings and lead to corrugation deformation. The EPC strength in MgB₂ is mainly contributed by the in-plane vibration mode of B atoms.⁷³ However, the situation is different in MoIrB_4 . The phonon mode with the largest line width among high-frequency phonons corresponds to the out-of-plane vibration of B atoms, as shown in Figure 4b. Moreover, Figure 4c shows that the EPC in MoIrB_4 is mainly from Ir atoms with ~60% contribution and only ~20% from B atoms. While the synthesis of stoichiometric MoIrB_4 was not reported, a few ReB₂-type ternary borides were briefly reported in the 1970s.^{74,75} More careful experimental investigations on these systems might reveal some superconductors. The Mo–Ir–B system has another ternary Mo_2IrB_2 phase, which was synthesized experimentally.⁷⁶ Vandenberg et al.⁶⁶ reported $T_c = 3.6$ K for the Mo_2IrB_2 compound. In our screening calculations, Mo_2IrB_2 did not pass our E filter because the

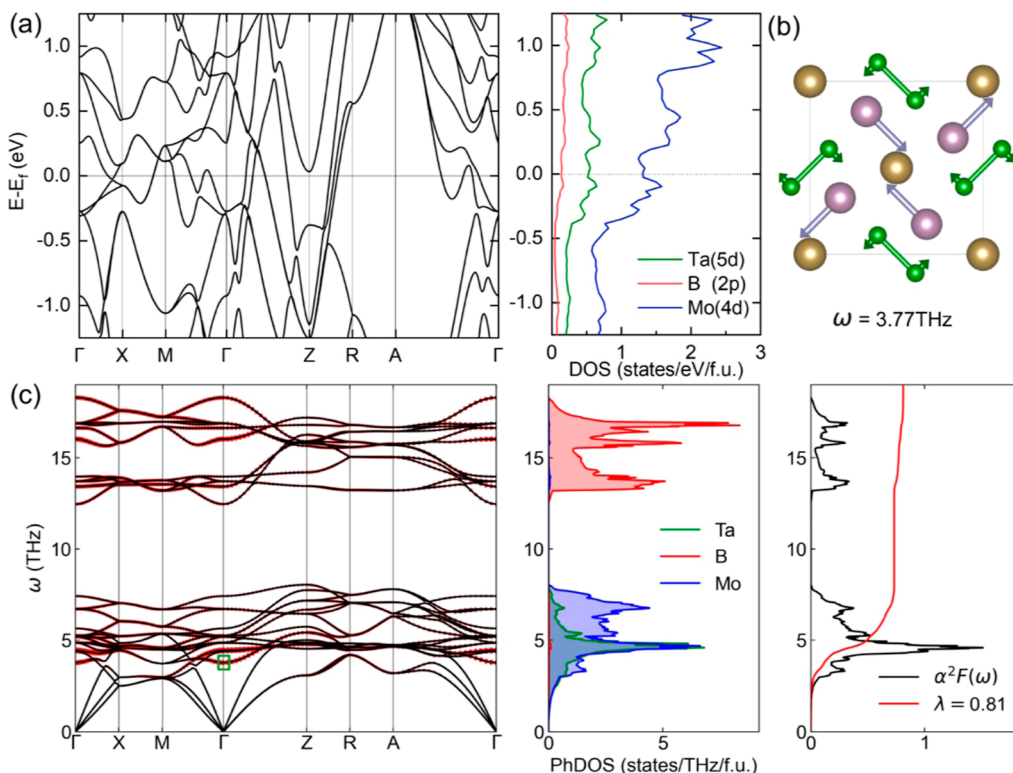


Figure 6. (a) Band structure and projected density of states of $TaMo_2B_2$. (b) Structure of $TaMo_2B_2$. The arrow represents the eigenvector of the phonon mode at the Γ point with a frequency of 3.8 THz, noted in (c). Purple is Mo, yellow is Ta, and green is B. (c) Phonon spectrum, projected phonon density of state, and the Eliashberg spectral function of $TaMo_2B_2$. The red bands on the phonon spectrum indicate the phonon line width.

zone-center modes made little contribution to the superconductivity in this compound.

3.3.3. $Ca_2Rh_5B_4$. The Rh atom in $Ca_2Rh_5B_4$ is coplanar with the four surrounding B atoms with Rh–B bond length $\sim 2.16\text{ \AA}$, forming a series of RhB_4 clusters. These clusters are connected by sharing Rh atoms to form a framework. Ca atoms are embedded in this matrix framework. This structure was first synthesized in 1983.⁵⁸ The band structure and phonon spectrum are shown in Figure 5a,c. Among B-dominated high-frequency phonons, the phonon mode with the largest phonon line width is the 26th mode at the Γ point ($\omega = 13.19\text{ THz}$), which is the breathing vibration of B atoms in the RhB_4 cluster, shown in Figure 5b. The DFPT result indicates that $Ca_2Rh_5B_4$ is a potential superconductor with $T_c = 4.9\text{ K}$ and $\lambda = 0.72$.

3.3.4. $TaMo_2B_2$. While Kuz'ma et al.⁵⁹ reported a solid solution phase for the $(Ta_{1-x}Mo_x)_3B_2$, we consider the ordered structure for the stoichiometric $TaMo_2B_2$ compound to investigate its superconductivity. The B_2 dumbbell in $TaMo_2B_2$ has a B–B bond length of $\sim 1.89\text{ \AA}$. Although the contribution of B-dominated high-frequency phonon modes to EPC strength is weak, phonon mode dominated by heavy elements in the low-frequency region contributes to large EPC. The T_c of $TaMo_2B_2$ is $\sim 12\text{ K}$ and $\lambda = 0.81$. One of the modes that contributes significantly to the EPC in the low-frequency region is the in-plane stretching vibration, primarily involving Mo atoms and, to a lesser extent, B atoms, as shown in Figure 6b. On the other hand, the high electron density of states benefits strong EPC. The van Hove singularity below the Fermi level may regulate the E_F by hole doping or induce high-frequency phonon modes to soften by element doping, which

provides a promising way to improve further the superconducting temperature of $TaMo_2B_2$.

We have shown that large-scale screening with fast EPC calculations can efficiently suggest potential conventional superconductors for future experimental investigations. By comparing the EPC constant between full Brillouin-zone DFPT calculations and the zone-center EPC strength in Table 1, we found a rather positive correlation, as shown in Figure S17. This correlation is similar to the one in hydrides identified previously.¹² However, in contrast to the unique hydrogen network found in high-pressure superconducting hydrides, the patterns of superconductivity in borides appear to be more diverse. The low-frequency phonon bands involving the metal and boron atoms contribute significantly to EPC in many boride structures. We also notice the limitation of the scheme: the EPC screening implemented in the E filter may overlook systems where the strong EPC is concentrated away from the Brillouin zone center, for example, in the Mo_2IrB_2 compound with experimental $T_c = 3.6\text{ K}$.⁷⁷ Such “false negative” cases are hard to avoid with our simplified EPC estimation but do not affect the accuracy of the predicted superconducting phases. Our calculations on the superconductivity are all based on the ordered structure, while experiments often resulted in solid solution phases. A careful design of synthetic paths can be crucial to realizing the predicted compounds.

4. CONCLUSIONS

In summary, by applying a series of filters to extract binary and ternary boride candidates from the crystal structural database, we identified 23 promising candidates as potential superconductors. Further DFPT calculations revealed their EPC and superconducting temperature. While superconductivity in

binary borides has been confirmed through experiments and computations, the superconductivity in ternary borides remains relatively unexplored. Notably, $TaMo_2B_2$ exhibits the highest superconducting temperature at approximately 12 K. Since most ternary compounds have been synthesized, the predicted superconductivity can be validated through future experiments. This study highlights the potential of utilizing high-throughput computational screening to discover new superconducting materials. Additionally, it demonstrates that, apart from the well-studied MgB_2 structure, diverse structural motifs in borides can lead to superconductivity. These motifs could be the foundation for future high-throughput screening involving elemental substitution to discover new compounds.

■ ASSOCIATED CONTENT

§ Supporting Information

The Supporting Information is available free of charge at <https://pubs.acs.org/doi/10.1021/acs.inorgchem.4c00159>.

Additional figures for zone-center EPC strength, phonon dispersion, phonon density of state, Eliashberg spectrum, and convergence test for the T_c calculations ([PDF](#))

■ AUTHOR INFORMATION

Corresponding Author

Yang Sun – Department of Physics, Xiamen University, Xiamen 361005, China;  orcid.org/0000-0002-4344-2920; Email: yangsun@xmu.edu.cn

Authors

Shiya Chen – Department of Physics, Xiamen University, Xiamen 361005, China

Zepeng Wu – Department of Physics, Xiamen University, Xiamen 361005, China

Zhen Zhang – Department of Physics, Iowa State University, Ames, Iowa 50011, United States;  orcid.org/0009-0001-0810-8054

Shunqing Wu – Department of Physics, Xiamen University, Xiamen 361005, China;  orcid.org/0000-0002-2545-0054

Kai-Ming Ho – Department of Physics, Iowa State University, Ames, Iowa 50011, United States

Vladimir Antropov – Ames National Laboratory, Ames, Iowa 50011, United States

Complete contact information is available at:

<https://pubs.acs.org/10.1021/acs.inorgchem.4c00159>

Notes

The authors declare no competing financial interest.

■ ACKNOWLEDGMENTS

The work at Xiamen University was supported by the Natural Science Foundation of Xiamen (grant no. 3502Z202371007) and the Fundamental Research Funds for the Central Universities (grant no. 20720230014). V.A. was supported by the U.S. Department of Energy, Office of Basic Energy Sciences, Division of Materials Sciences and Engineering. The Ames National Laboratory is operated for the U.S. Department of Energy by the Iowa State University under contract no. DE-AC02-07CH11358. K.-M.H. acknowledges support from the National Science Foundation, award no. DMR2132666. Shaorong Fang and Tianfu Wu from the Information and

Network Center of Xiamen University are acknowledged for their help with graphics processing unit (GPU) computing.

■ REFERENCES

- (1) Choudhary, K.; Garrity, K. Designing High-TC Superconductors with BCS-Inspired Screening, Density Functional Theory, and Deep-Learning. *npj Comput. Mater.* **2022**, *8* (1), 244.
- (2) Flores-Livas, J. A.; Boeri, L.; Sanna, A.; Profeta, G.; Arita, R.; Eremets, M. A Perspective on Conventional High-Temperature Superconductors at High Pressure: Methods and Materials. *Phys. Rep.* **2020**, *856*, 1–78.
- (3) Hoffmann, N.; Cerqueira, T. F. T.; Schmidt, J.; Marques, M. A. L. Superconductivity in Antiperovskites. *npj Comput. Mater.* **2022**, *8* (1), 150.
- (4) Pogue, E. A.; New, A.; McElroy, K.; Le, N. Q.; Pekala, M. J.; McCue, I.; Gienger, E.; Domenico, J.; Hedrick, E.; McQueen, T. M.; et al. Closed-Loop Superconducting Materials Discovery. *npj Comput. Mater.* **2023**, *9*, 181.
- (5) Cerqueira, T. F. T.; Sanna, A.; Marques, M. A. L. Sampling the Materials Space for Conventional Superconducting Compounds. *Adv. Mater.* **2024**, *36* (1), 2307085.
- (6) Nagamatsu, J.; Nakagawa, N.; Muranaka, T.; Zenitani, Y.; Akimitsu, J. Superconductivity at 39 K in Magnesium Diboride. *Nature* **2001**, *410* (6824), 63–64.
- (7) Kortus, J.; Mazin, I. I.; Belashchenko, K. D.; Antropov, V. P.; Boyer, L. L. Superconductivity of Metallic Boron in MgB_2 . *Phys. Rev. Lett.* **2001**, *86* (20), 4656–4659.
- (8) Pallecchi, I.; Brotto, P.; Ferdeghini, C.; Putti, M.; Palenzona, A.; Manfrinetti, P.; Geddo Lehmann, A.; Orecchini, A.; Petrillo, C.; Sacchetti, F.; Afronne, M.; Allodi, G.; De Renzi, R.; Serventi, S.; Andreone, A.; Lamura, G.; Daghero, D.; Gonnelli, R. S.; Tortello, M. Investigation of Li-Doped MgB_2 . *Supercond. Sci. Technol.* **2009**, *22* (9), 095014.
- (9) Feng, Y.; Zhao, Y.; Pradhan, A. K.; Cheng, C. H.; Yau, J. K. F.; Zhou, L.; Koshizuka, N.; Murakami, M. Enhanced Flux Pinning in Zr-Doped MgB_2 Bulk Superconductors Prepared at Ambient Pressure. *J. Appl. Phys.* **2002**, *92* (5), 2614–2619.
- (10) Pei, C.; Zhang, J.; Wang, Q.; Zhao, Y.; Gao, L.; Gong, C.; Tian, S.; Luo, R.; Li, M.; Yang, W.; Lu, Z.-Y.; Lei, H.; Liu, K.; Qi, Y. Pressure-Induced Superconductivity at 32 K in MoB_2 . *Natl. Sci. Rev.* **2023**, *10* (5), nwad034.
- (11) Lim, J.; Hire, A. C.; Quan, Y.; Kim, J. S.; Xie, S. R.; Sinha, S.; Kumar, R. S.; Popov, D.; Park, C.; Hemley, R. J.; Vohra, Y. K.; Hamlin, J. J.; Hennig, R. G.; Hirschfeld, P. J.; Stewart, G. R. Creating Superconductivity in WB_2 through Pressure-Induced Metastable Planar Defects. *Nat. Commun.* **2022**, *13* (1), 7901.
- (12) Sun, Y.; Zhang, F.; Wang, C.-Z.; Ho, K.-M.; Mazin, I. I.; Antropov, V. Electron-Phonon Coupling Strength from *Ab Initio* Frozen-Phonon Approach. *Phys. Rev. Mater.* **2022**, *6* (7), 074801.
- (13) Wang, R.; Sun, Y.; Zhang, F.; Zheng, F.; Fang, Y.; Wu, S.; Dong, H.; Wang, C.-Z.; Antropov, V.; Ho, K.-M. High-Throughput Screening of Strong Electron-Phonon Couplings in Ternary Metal Diborides. *Inorg. Chem.* **2022**, *61* (45), 18154–18161.
- (14) Wu, Z.; Sun, Y.; Durajski, A. P.; Zheng, F.; Antropov, V.; Ho, K.-M.; Wu, S. Effect of Doping on the Phase Stability and Superconductivity in LaH_{10} . *Phys. Rev. Mater.* **2023**, *7* (10), L101801.
- (15) Zheng, F.; Sun, Y.; Wang, R.; Fang, Y.; Zhang, F.; Wu, S.; Wang, C.-Z.; Antropov, V.; Ho, K.-M. Superconductivity in the Li-B-C System at 100 GPa. *Phys. Rev. B* **2023**, *107* (1), 014508.
- (16) Zheng, F.; Sun, Y.; Wang, R.; Fang, Y.; Zhang, F.; Wu, S.; Lin, Q.; Wang, C.-Z.; Antropov, V.; Ho, K.-M. Prediction of Superconductivity in Metallic Boron-Carbon Compounds from 0 to 100 GPa by High-Throughput Screening. *Phys. Chem. Chem. Phys.* **2023**, *25* (47), 32594–32601.
- (17) Sun, Y.; Zhang, Z.; Porter, A. P.; Kovnir, K.; Ho, K.-M.; Antropov, V. Prediction of Van Hove Singularity Systems in Ternary Borides. *npj Comput. Mater.* **2023**, *9* (1), 204.
- (18) Blöchl, P. E. Projector Augmented-Wave Method. *Phys. Rev. B: Condens. Matter Mater. Phys.* **1994**, *50* (24), 17953–17979.

- (19) Kresse, G.; Furthmüller, J. Efficiency of Ab-Initio Total Energy Calculations for Metals and Semiconductors Using a Plane-Wave Basis Set. *Comput. Mater. Sci.* **1996**, *6* (1), 15–50.
- (20) Kresse, G.; Furthmüller, J. Efficient Iterative Schemes for Ab Initio Total-Energy Calculations Using a Plane-Wave Basis Set. *Phys. Rev. B: Condens. Matter Mater. Phys.* **1996**, *54* (16), 11169–11186.
- (21) Perdew, J. P.; Burke, K.; Ernzerhof, M. Generalized Gradient Approximation Made Simple. *Phys. Rev. Lett.* **1996**, *77* (18), 3865–3868.
- (22) Monkhorst, H. J.; Pack, J. D. Special Points for Brillouin-Zone Integrations. *Phys. Rev. B: Solid State* **1976**, *13* (12), 5188–5192.
- (23) Jain, A.; Ong, S. P.; Hautier, G.; Chen, W.; Richards, W. D.; Dacek, S.; Cholia, S.; Gunter, D.; Skinner, D.; Ceder, G.; Persson, K. A. Commentary: The Materials Project: A Materials Genome Approach to Accelerating Materials Innovation. *APL Mater.* **2013**, *1* (1), 011002.
- (24) Togo, A.; Tanaka, I. First Principles Phonon Calculations in Materials Science. *Scr. Mater.* **2015**, *108*, 1–5.
- (25) Baroni, S.; de Gironcoli, S.; Dal Corso, A.; Giannozzi, P. Phonons and Related Crystal Properties from Density-Functional Perturbation Theory. *Rev. Mod. Phys.* **2001**, *73* (2), 515–562.
- (26) Giannozzi, P.; Andreussi, O.; Brumme, T.; Bunau, O.; Buongiorno Nardelli, M.; Calandra, M.; Car, R.; Cavazzoni, C.; Ceresoli, D.; Cococcioni, M.; Colonna, N.; Carnimeo, I.; Dal Corso, A.; de Gironcoli, S.; Delugas, P.; DiStasio, R. A.; Ferretti, A.; Floris, A.; Fratesi, G.; Fugallo, G.; Gebauer, R.; Gerstmann, U.; Giustino, F.; Gorni, T.; Jia, J.; Kawamura, M.; Ko, H.-Y.; Kokalj, A.; Küçükbenli, E.; Lazzeri, M.; Marsili, M.; Marzari, N.; Mauri, F.; Nguyen, N. L.; Nguyen, H.-V.; Otero-de-la-Roza, A.; Paulatto, L.; Poncé, S.; Rocca, D.; Sabatini, R.; Santra, B.; Schlipf, M.; Seitsonen, A. P.; Smogunov, A.; Timrov, I.; Thonhauser, T.; Umari, P.; Vast, N.; Wu, X.; Baroni, S. Advanced Capabilities for Materials Modelling with Quantum ESPRESSO. *J. Phys.: Condens. Matter* **2017**, *29* (46), 465901.
- (27) Giannozzi, P.; Baseggio, O.; Bonfa, P.; Brunato, D.; Car, R.; Carnimeo, I.; Cavazzoni, C.; de Gironcoli, S.; Delugas, P.; Ferrari Ruffino, F.; Ferretti, A.; Marzari, N.; Timrov, I.; Urru, A.; Baroni, S. Quantum ESPRESSO toward the Exascale. *J. Chem. Phys.* **2020**, *152* (15), 154105.
- (28) Dal Corso, A. Pseudopotentials Periodic Table: From H to Pu. *Comput. Mater. Sci.* **2014**, *95*, 337–350.
- (29) McMillan, W. L. Transition Temperature of Strong-Coupled Superconductors. *Phys. Rev.* **1968**, *167* (2), 331–344.
- (30) Allen, P. B.; Dynes, R. C. Transition Temperature of Strong-Coupled Superconductors Reanalyzed. *Phys. Rev. B: Solid State* **1975**, *12* (3), 905–922.
- (31) Allen, P. B. Neutron Spectroscopy of Superconductors. *Phys. Rev. B: Solid State* **1972**, *6* (7), 2577–2579.
- (32) Jain, A.; Montoya, J.; Dwaraknath, S.; Zimmermann, N. E. R.; Dagdelen, J.; Horton, M.; Huck, P.; Winston, D.; Cholia, S.; Ong, S. P.; Persson, K. The Materials Project: Accelerating Materials Design Through Theory-Driven Data and Tools. *Handbook of Materials Modeling*; Springer, 2018; pp 1–34.
- (33) Sun, Y.; Zhang, F.; Wu, S.; Antropov, V.; Ho, K.-M. Effect of Nitrogen Doping and Pressure on the Stability of LuH₃. *Phys. Rev. B* **2023**, *108* (2), L020101.
- (34) Belsky, A.; Hellenbrandt, M.; Karen, V. L.; Luksch, P. New Developments in the Inorganic Crystal Structure Database (ICSD): Accessibility in Support of Materials Research and Design. *Acta Crystallogr., Sect. B: Struct. Sci.* **2002**, *58* (3), 364–369.
- (35) Calandra, M.; Vast, N.; Mauri, F. Superconductivity from Doping Boron Icosahedra. *Phys. Rev. B: Condens. Matter Mater. Phys.* **2004**, *69* (22), 224505.
- (36) Will, G.; Kossobutzki, K. H. An X-Ray Diffraction Analysis of Boron Carbide, B₁₃C₂. *J. Less-Common Met.* **1976**, *47*, 43–48.
- (37) Shirai, K.; Sakuma, K.; Uemura, N. Theoretical Study of the Structure of Boron Carbide B₁₃C₂. *Phys. Rev. B: Condens. Matter Mater. Phys.* **2014**, *90* (6), 064109.
- (38) Kennard, C. H. L.; Davis, L. Zirconium Dodecarborides ZrB₁₂: Confirmation of the B₁₂ Cubooctahedral Unit. *J. Solid State Chem.* **1983**, *47* (1), 103–106.
- (39) Wang, Y.; Lortz, R.; Paderno, Y.; Filippov, V.; Abe, S.; Tutsch, U.; Junod, A. Specific Heat and Magnetization of a ZrB₁₂ Single Crystal: Characterization of a Type-II/1 Superconductor. *Phys. Rev. B: Condens. Matter Mater. Phys.* **2005**, *72* (2), 024548.
- (40) Ammar, A.; Ménétrier, M.; Villesuzanne, A.; Matar, S.; Chevalier, B.; Etourneau, J.; Villeneuve, G.; Rodríguez-Carvajal, J.; Koo, H.-J.; Smirnov, A. I.; Whangbo, M.-H. Investigation of the Electronic and Structural Properties of Potassium Hexaboride, KB₆, by Transport, Magnetic Susceptibility, EPR, and NMR Measurements, Temperature-Dependent Crystal Structure Determination, and Electronic Band Structure Calculations. *Inorg. Chem.* **2004**, *43* (16), 4974–4987.
- (41) Katsura, Y.; Yamamoto, A.; Ogino, H.; Horii, S.; Shimoyama, J.; Kishio, K.; Takagi, H. On the Possibility of MgB₂-like Superconductivity in Potassium Hexaboride. *Phys. C* **2010**, *470*, S633–S634.
- (42) Havinga, E. E.; Damsma, H.; Hokkeling, P. Compounds and Pseudo-Binary Alloys with the CuAl₂(C16)-Type Structure I. Preparation and X-Ray Results. *J. Less-Common Met.* **1972**, *27* (2), 169–186.
- (43) Ge, Y.; Bao, K.; Ma, T.; Zhang, J.; Zhou, C.; Ma, S.; Tao, Q.; Zhu, P.; Cui, T. Revealing the Unusual Boron-Pinned Layered Substructure in Superconducting Hard Molybdenum Semiboride. *ACS Omega* **2021**, *6* (33), 21436–21443.
- (44) Hardy, G. F.; Hulm, J. K. The Superconductivity of Some Transition Metal Compounds. *Phys. Rev.* **1954**, *93* (5), 1004–1016.
- (45) Kayhan, M. Transition Metal Borides: Synthesis, Characterization and Superconducting Properties. Ph.D. Thesis, Technische Universität, Darmstadt, 2013. <https://tuprints.ulb.tu-darmstadt.de/3613/> (accessed 2023–08–28).
- (46) Singh, P. P. Theoretical Study of Electron-Phonon Interaction in ZrB₂ and TaB₂. *Phys. Rev. B: Condens. Matter Mater. Phys.* **2004**, *69* (9), 094519.
- (47) Yu, Z.; Bo, T.; Liu, B.; Fu, Z.; Wang, H.; Xu, S.; Xia, T.; Li, S.; Meng, S.; Liu, M. Superconductive Materials with MgB₂-like Structures from Data-Driven Screening. *Phys. Rev. B* **2022**, *105* (21), 214517.
- (48) Sichkar, S. M.; Antonov, V. N. Electronic Structure, Phonon Spectra and Electron-Phonon Interaction in ScB₂. *Low Temp. Phys.* **2013**, *39* (7), 595–601.
- (49) Jones, M. E.; Marsh, R. E. The Preparation and Structure of Magnesium Boride, MgB₂. *J. Am. Chem. Soc.* **1954**, *76* (5), 1434–1436.
- (50) Norton, J. T.; Blumenthal, H.; Sindeband, S. J. Structure of Diborides of Titanium, Zirconium, Columbium, Tantalum and Vanadium. *JOM* **1949**, *1* (10), 749–751.
- (51) Kuz'ma, Yu. B.; Lakh, V. I.; Stadnyk, B. I.; Voroshikov, Yu. V. X-Ray Diffraction Study of the System Niobium-Tungsten-Boron. *Powder Metall. Met. Ceram.* **1966**, *5* (6), 491–493.
- (52) Waśkowska, A.; Gerward, L.; Staun Olsen, J.; Ramesh Babu, K.; Vaitheswaran, G.; Kanchana, V.; Svane, A.; Filipov, V. B.; Levchenko, G.; Lysachenko, A. Thermoelastic Properties of ScB₂, TiB₂, YB₄ and HoB₄: Experimental and Theoretical Studies. *Acta Mater.* **2011**, *59* (12), 4886–4894.
- (53) Kaczorowski, D.; Zaleski, A. J.; Żogal, O. J.; Klamut, J. Incipient Superconductivity in TaB₂. *arXiv* **2001**, arXiv:cond-mat/0103571. <http://arxiv.org/abs/cond-mat/0103571> (accessed 2023–08–19)
- (54) Moussa, J. E.; Noffsinger, J.; Cohen, M. L. Possible Thermodynamic Stability and Superconductivity of Antifluorite Be₂B_xC_{1-x}. *Phys. Rev. B: Condens. Matter Mater. Phys.* **2008**, *78* (10), 104506.
- (55) Sands, D. E.; Cline, C. F.; Zalkin, A.; Hoenig, C. L. The Beryllium-Boron System. *Acta Crystallogr.* **1961**, *14* (3), 309–310.
- (56) Garvie, L. A. J.; Hubert, H.; Petuskey, W. T.; McMillan, P. F.; Buseck, P. R. High-Pressure, High-Temperature Syntheses in the B-C-N-O System. *J. Solid State Chem.* **1997**, *133* (2), 365–371.

- (57) Shelton, R. N. Superconductivity and Crystal Structure of a New Class of Ternary Platinum Borides. *J. Less-Common Met.* **1978**, *62*, 191–196.
- (58) Jung, W. $A_nRh_{3n-1}B_{2n}$ Mit A \equiv Ca Und Sr, Eine Homologe Reihe Ternärer Erdalkali-Rhodiumboride Aus Bauelementen Der $CeCo_3B_2$ - Und Der $CaRh_2B_2$ -Struktur. *J. Less-Common Met.* **1984**, *97*, 253–263.
- (59) Sobolev, A. S.; Kuz'ma, Yu. B.; Soboleva, T. E.; Fedorov, T. F. Phase Equilibria in Tantalum — Titanium — Boron and Tantalum — Molybdenum — Boron Systems. *Powder Metall. Met. Ceram.* **1968**, *7* (1), 48–51.
- (60) Kuz'ma, Yu. B. An X-Ray Structural Investigation of the Systems Niobium-Titanium-Boron and Niobium-Molybdenum-Boron. *Powder Metall. Met. Ceram.* **1971**, *10* (4), 298–300.
- (61) Jung, W. Ternäre Seltenerd-Iridiumboride $SEIr_3B_2$ ($SE \equiv Y, La, Ce, Pr, Nd, Sm, Eu, Gd, Tb, Dy$) Mit $CaRh_2B_2$ -Struktur. *J. Less-Common Met.* **1991**, *171* (1), 119–125.
- (62) Sampathkumaran, E. V.; Das, I. Magnetic Behavior of $CeIr_2B_2$. *Phys. Rev. B: Condens. Matter Mater. Phys.* **1995**, *51* (13), 8628–8630.
- (63) Bolotina, N. B.; Khrykina, O. N.; Azarevich, A. N.; Shitsevalova, N. Yu.; Filipov, V. B.; Gavrilkin, S. Yu.; Mitsen, K. V.; Voronov, V. V.; Sluchanko, N. E. Checkerboard Patterns of Charge Stripes in the Two-Gap Superconductor ZrB . *Phys. Rev. B* **2022**, *105* (5), 054511.
- (64) Sekar, M.; Chandra Shekar, N. V.; Appalakondaiah, S.; Shwetha, G.; Vaiteeswaran, G.; Kanchana, V. Structural Stability of Ultra-Incompressible Mo_2B : A Combined Experimental and Theoretical Study. *J. Alloys Compd.* **2016**, *654*, 554–560.
- (65) Sun, T.; Zhang, D.-B.; Wentzcovitch, R. M. Dynamic Stabilization of Cubic $CaSiO_3$ Perovskite at High Temperatures and Pressures from *Ab Initio* Molecular Dynamics. *Phys. Rev. B: Condens. Matter Mater. Phys.* **2014**, *89* (9), 094109.
- (66) Wu, Y.-N.; Saidi, W. A.; Wuenschell, J. K.; Tadano, T.; Ohodnicki, P.; Chorpening, B.; Duan, Y. Anharmonicity Explains Temperature Renormalization Effects of the Band Gap in $SrTiO_3$. *J. Phys. Chem. Lett.* **2020**, *11*, 2518–2523.
- (67) Yue, T.; Zhao, Y.; Ni, J.; Meng, S.; Dai, Z. Strong Quartic Anharmonicity, Ultralow Thermal Conductivity, High Band Degeneracy and Good Thermoelectric Performance in Na_2TlSb . *npj Comput. Mater.* **2023**, *9* (1), 17.
- (68) Wang, M.; Liu, C.; Wen, M.; Li, Q.; Ma, Y. Investigations on Structural Determination of Semi-Transition-Metal Borides. *Phys. Chem. Chem. Phys.* **2017**, *19* (47), 31592–31598.
- (69) Shein, I. R.; Ivanovskii, A. L. Superconductivity in Be₂B? Comparative Analysis of the Band Structure of MgB_2 , BeB_2 and Be_2B . *Phys. Status Solidi B* **2001**, *227* (2), R1–R3.
- (70) Ku, H. C.; Meisner, G. P. Crystal Structure and Physical Properties of New Ternary Rare Earth Borides. *J. Less-Common Met.* **1981**, *78* (1), 99–107.
- (71) Ferreira, P. P.; Conway, L. J.; Cucciari, A.; Di Cataldo, S.; Giannessi, F.; Kogler, E.; Eleno, L. T. F.; Pickard, C. J.; Heil, C.; Boeri, L. Search for Ambient Superconductivity in the Lu-N-H System. *Nat. Commun.* **2023**, *14* (1), 5367.
- (72) Choi, H. J.; Roundy, D.; Sun, H.; Cohen, M. L.; Louie, S. G. The Origin of the Anomalous Superconducting Properties of MgB_2 . *Nature* **2002**, *418* (6899), 758–760.
- (73) Rogl, P.; Nowotny, H.; Benesovsky, F. Komplexboride mit ReB_2 -Struktur. *Monatsh. Chem.* **1970**, *101* (1), 27–31.
- (74) Rogl, P.; Nowotny, H.; Benesovsky, F. Ternäre Komplexboride in den Dreistoffen: {Mo, W}-{Ru, Os}-B und W-Ir-B. *Monatsh. Chem.* **1970**, *101* (3), 850–854.
- (75) Rogl, P.; Benesovsky, F.; Nowotny, H. Über einige Komplexboride mit Platinmetallen. *Monatsh. Chem.* **1972**, *103* (4), 965–989.
- (76) Vandenberg, J. M.; Matthias, B. T.; Corenzvit, E.; Barz, H. Superconductivity of Some Binary and Ternary Transition-Metal Borides. *Mater. Res. Bull.* **1975**, *10* (9), 889–894.
- (77) Chen, S.; Wu, Z.; Zhang, Z.; Wu, S.; Ho, K. M.; Antropov, A.; Sun, Y. High-throughput screening for boride superconductors. *arXiv* (*PhysicsCondensed Matter*) **2024**, arXiv:2401.13211. (accessed 2024-01-24)

Supporting Information

High-throughput screening for boride superconductors

Shiya Chen¹, Zepeng Wu¹, Zhen Zhang², Shunqing Wu¹, Kai-Ming Ho², Vladimir Antropov³ and Yang Sun^{1*}

¹Department of Physics, Xiamen University, Xiamen 361005, China

²Department of Physics, Iowa State University, Ames, Iowa 50011, USA

³Ames National Laboratory, Ames, Iowa 50011, USA

Contents

Figure S1-S18

*Email: yangsun@xmu.edu.cn

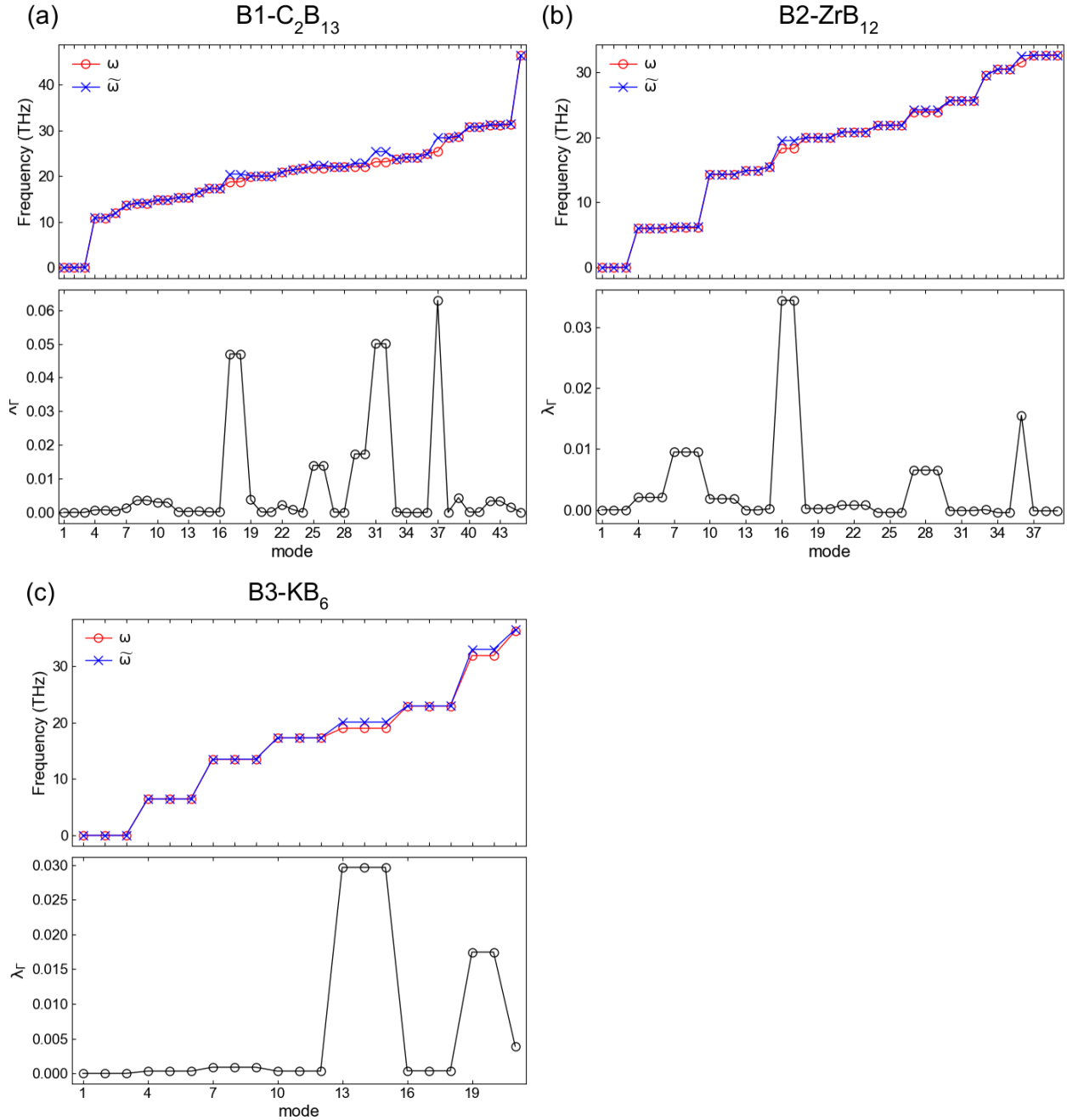


Fig. S1. The screened and unscreened phonon frequency (top panel) and zone-center EPC strength (bottom panel) in (a) B1-C₁₃B₂, (b) B2- ZrB₁₂ and (c) B3-KB₆

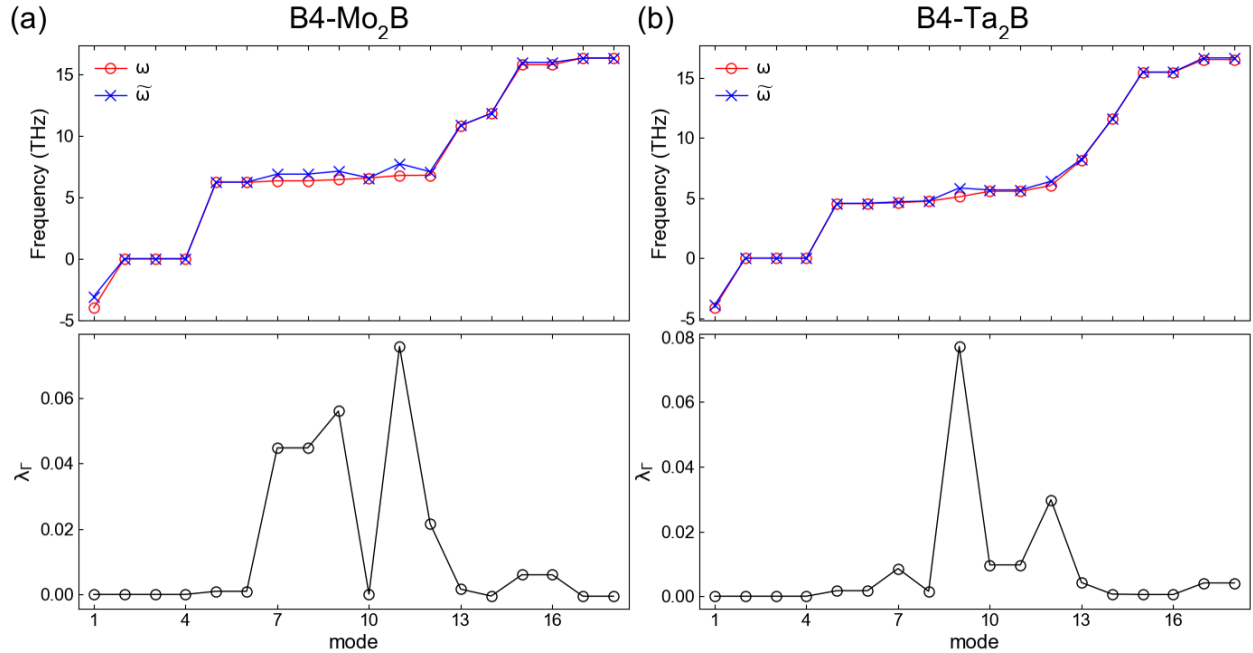


Fig. S2. The screened and unscreened phonon frequency (top panel) and zone-center EPC strength (bottom panel) in (a) B4-Mo₂B and (b) B4-Ta₂B.

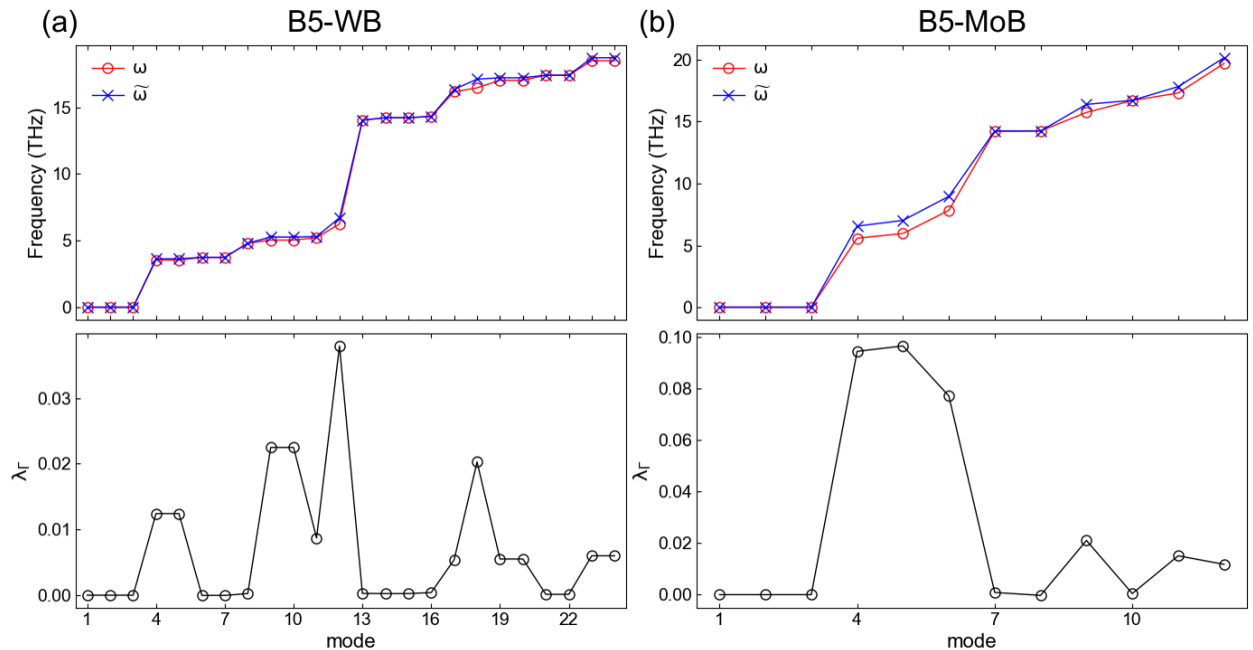


Fig. S3. The screened and unscreened phonon frequency (top panel) and zone-center EPC strength (bottom panel) in (a) B5-WB and (b) B5-MoB.

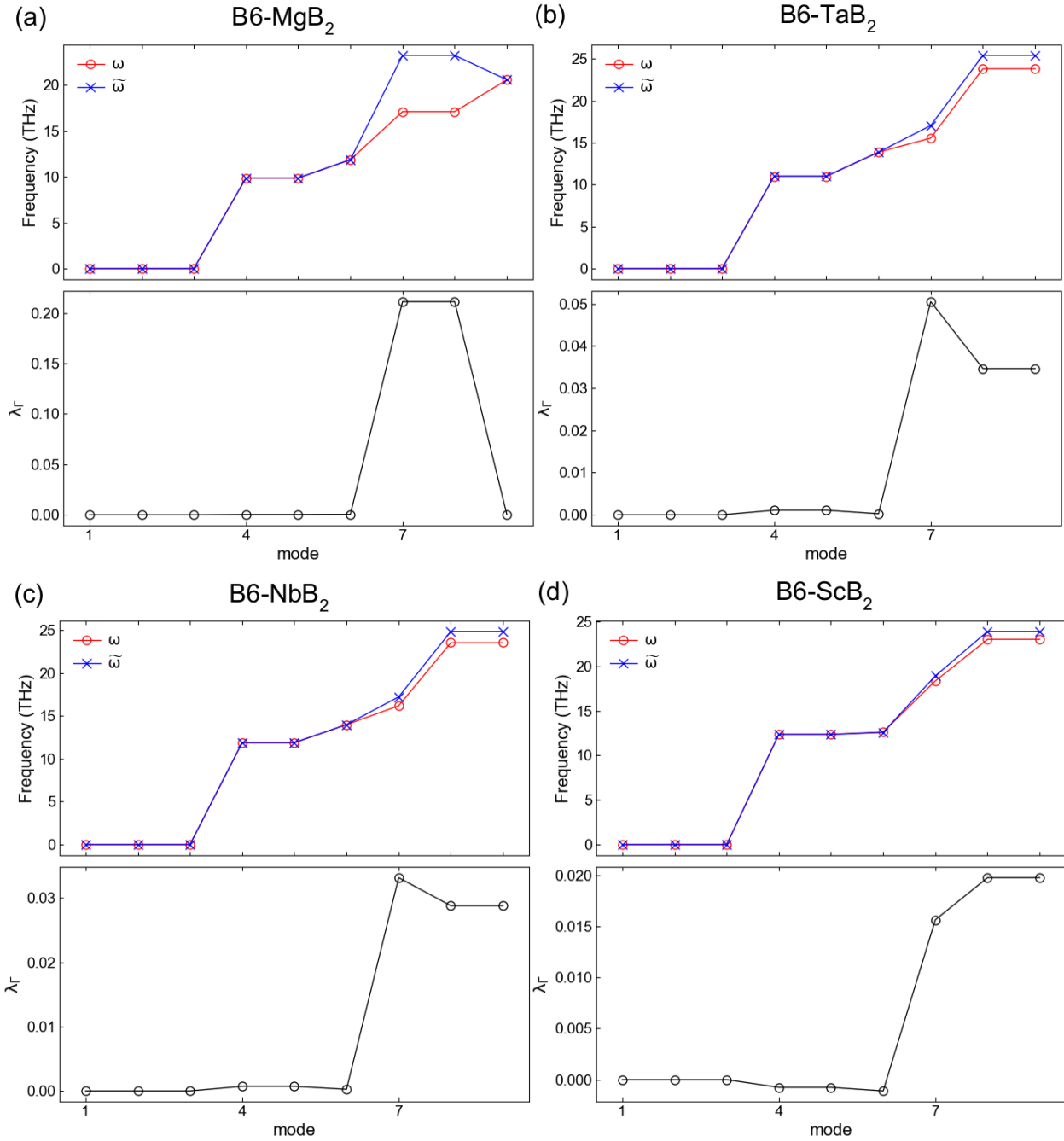


Fig. S4. The screened and unscreened phonon frequency (top panel) and zone-center EPC strength (bottom panel) in (a) B6-MgB₂, (b) B6-TaB₂, (c) B6-NbB₂, and (d) B6-ScB₂.

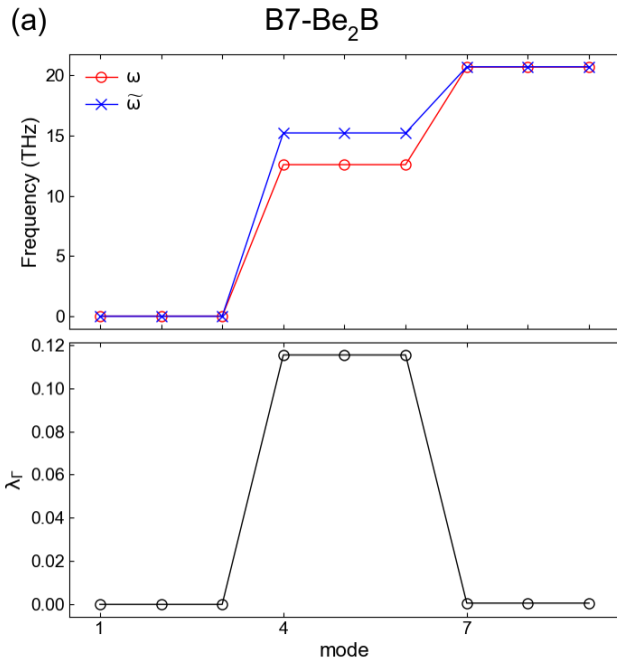


Fig. S5. The screened and unscreened phonon frequency (top panel) and zone-center EPC strength (bottom panel) in (a) B7-Be₂B.

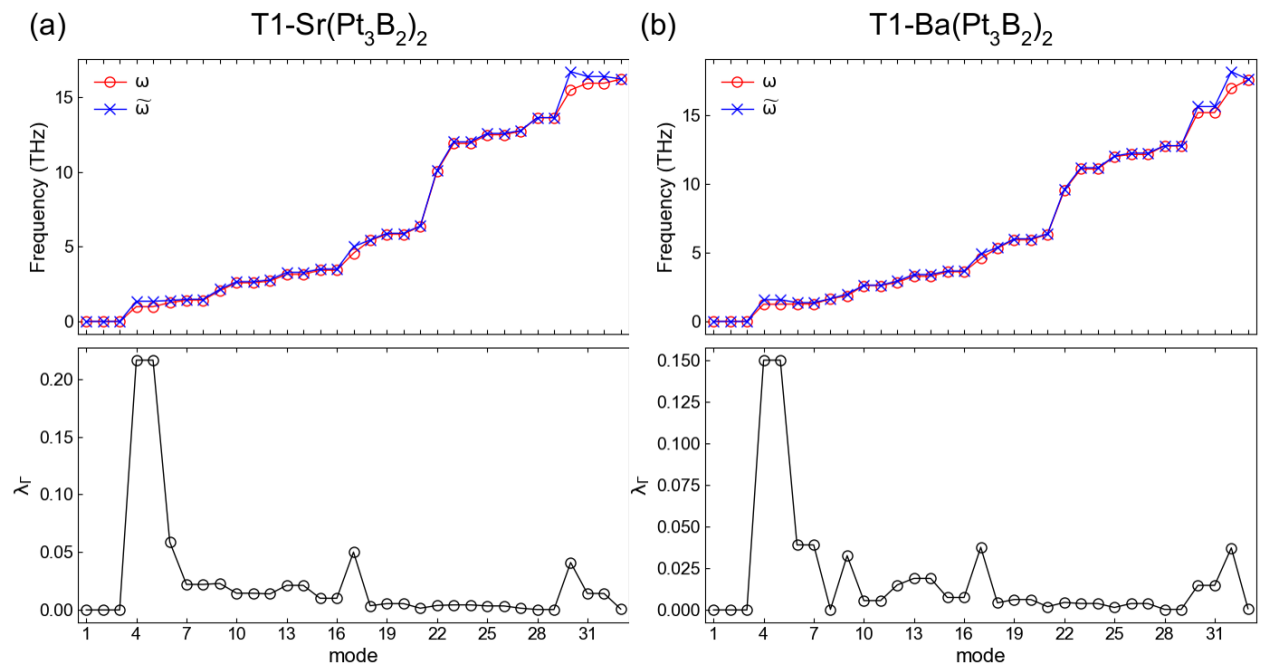


Fig. S6. The screened and unscreened phonon frequency (top panel) and zone-center EPC strength (bottom panel) in (a) T1-Sr(Pt₃B₂)₂ and (b) T1-Ba(Pt₃B₂)₂.

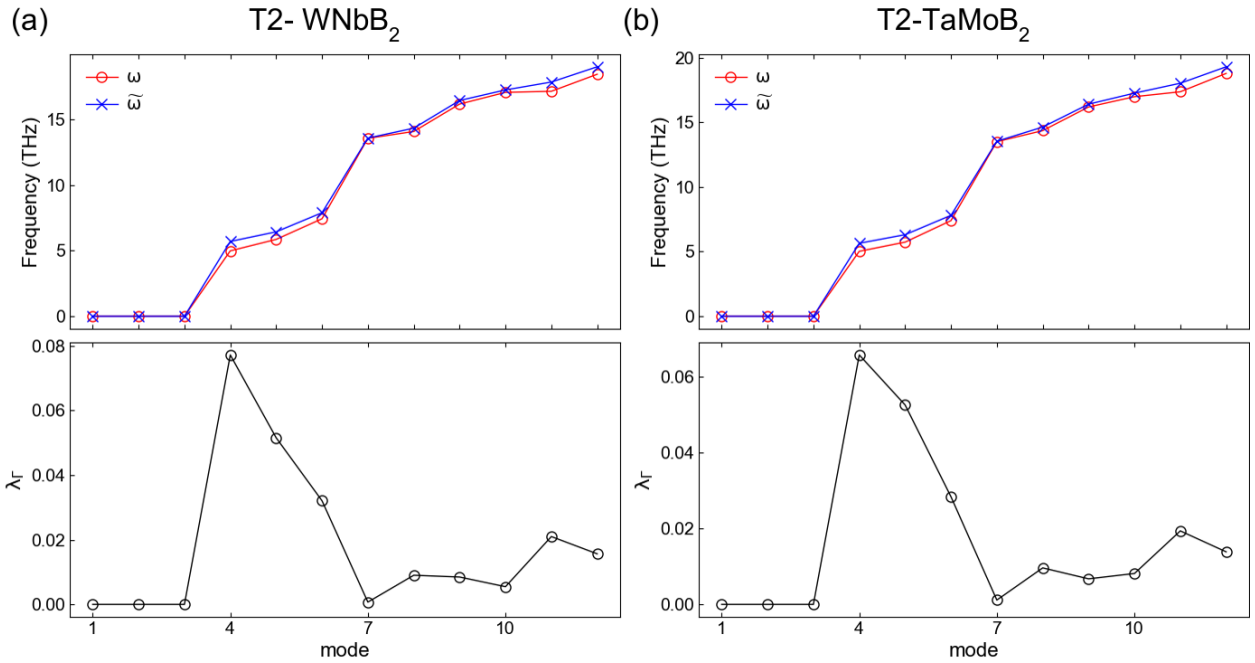


Fig. S7. The screened and unscreened phonon frequency (top panel) and zone-center EPC strength (bottom panel) in (a) T2-WNbB₂ and (b) T2-TaMoB₂.

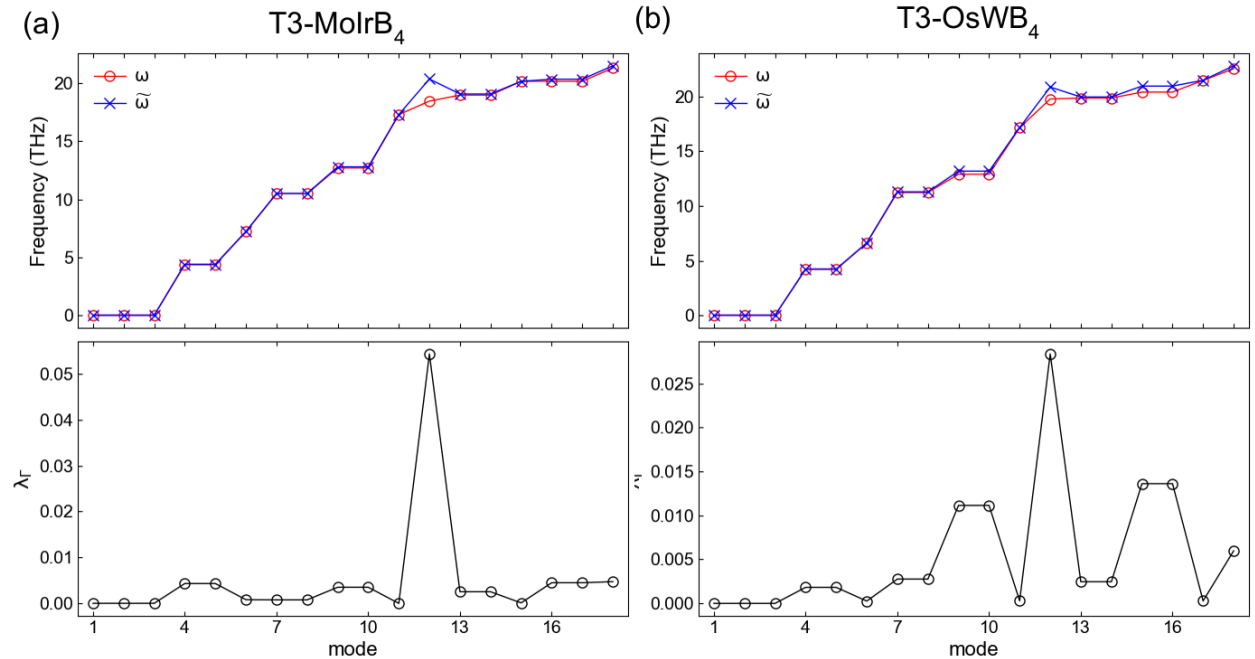


Fig. S8. The screened and unscreened phonon frequency (top panel) and zone-center EPC strength (bottom panel) in (a) T3-MoIrB₄ and (b) T3-OsWB₄.

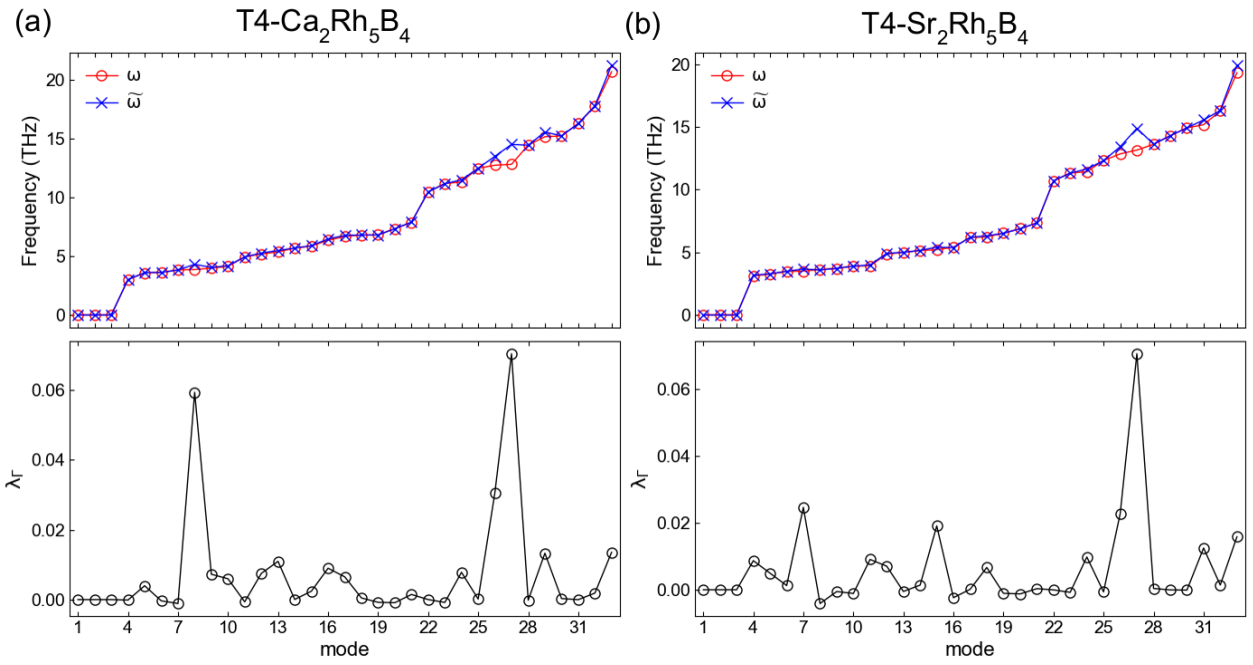


Fig. S9. The screened and unscreened phonon frequency (top panel) and zone-center EPC strength (bottom panel) in (a) T4-Ca₂Rh₅B₄ and (b) T4-Sr₂Rh₅B₄.

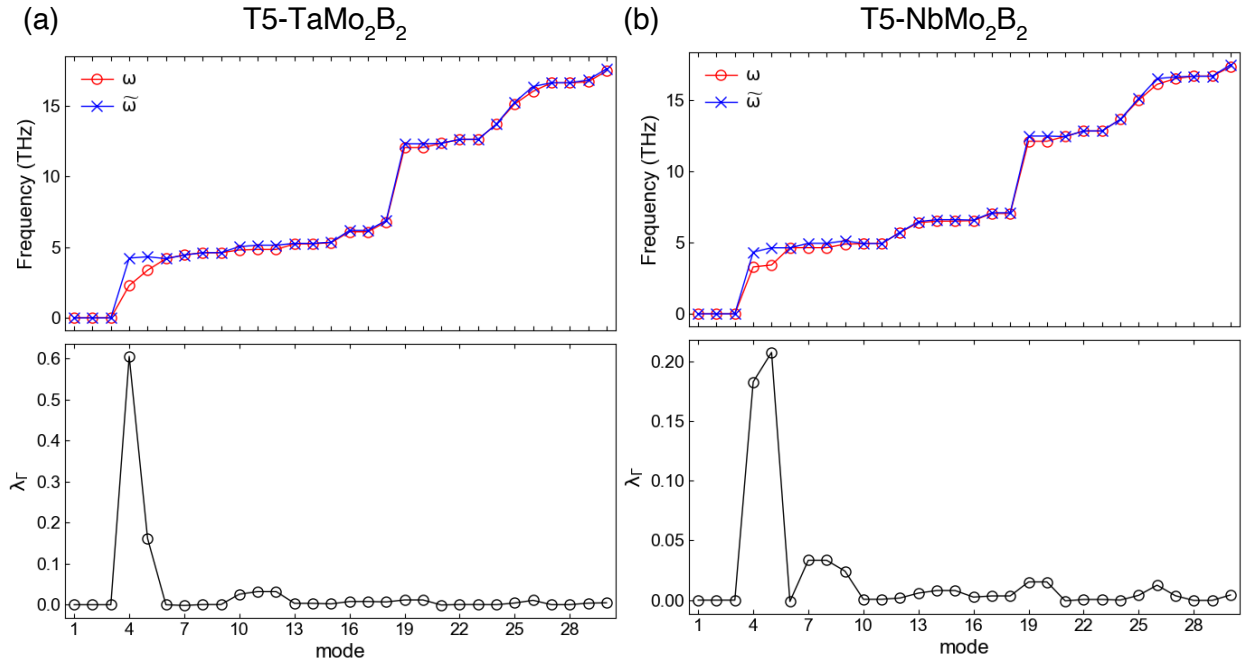


Fig. S10. The screened and unscreened phonon frequency (top panel) and zone-center EPC strength (bottom panel) in (a) T5-TaMo₂B₂ and (b) T5-NbMo₂B₂.

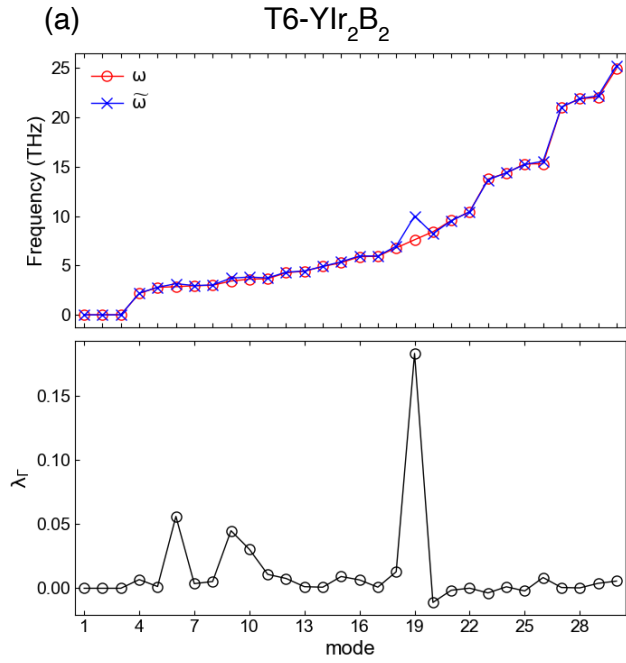


Fig. S11. The screened and unscreened phonon frequency (top panel) and zone-center EPC strength (bottom panel) in (a) T6-YIr₂B₂.

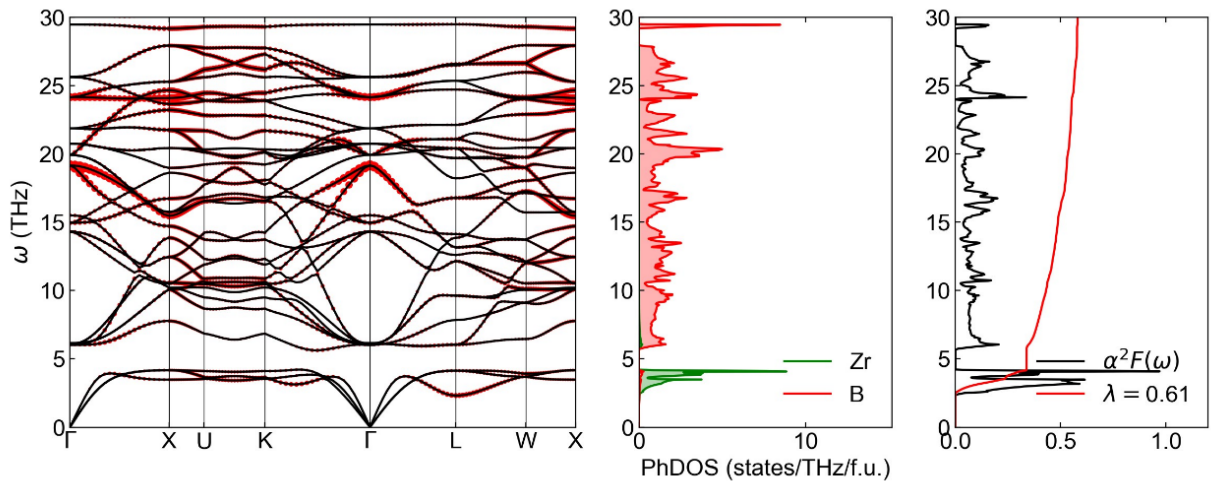


Fig. S12. Phonon dispersion, phonon density of state, and Eliashberg spectrum of ZrB₁₂. The red bands on the phonon dispersion indicate the strength of EPC.

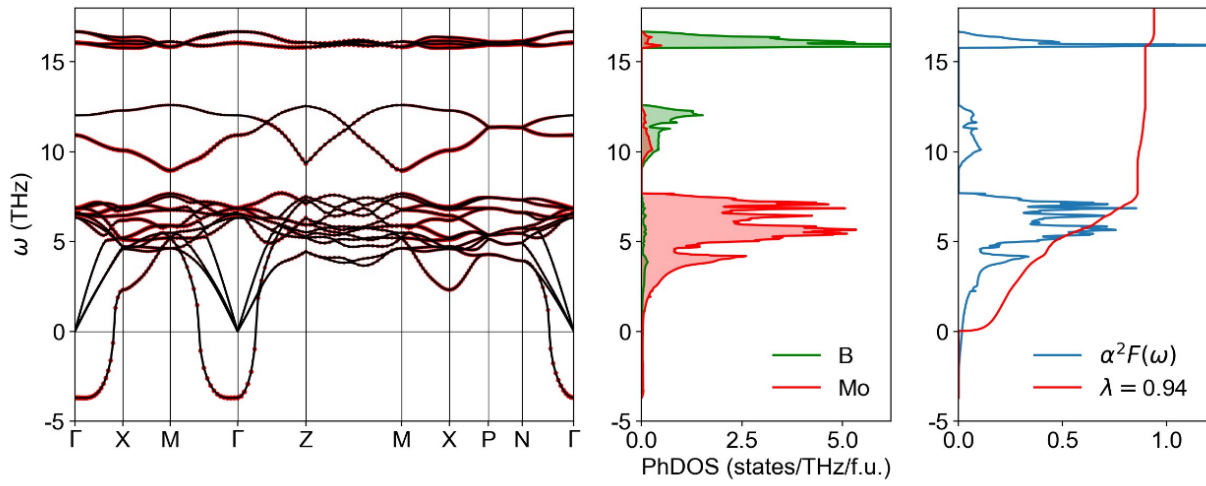


Fig. S13. Phonon dispersion, phonon density of state, and Eliashberg spectrum of Mo_2B . The red bands on the phonon dispersion indicate the strength of EPC.

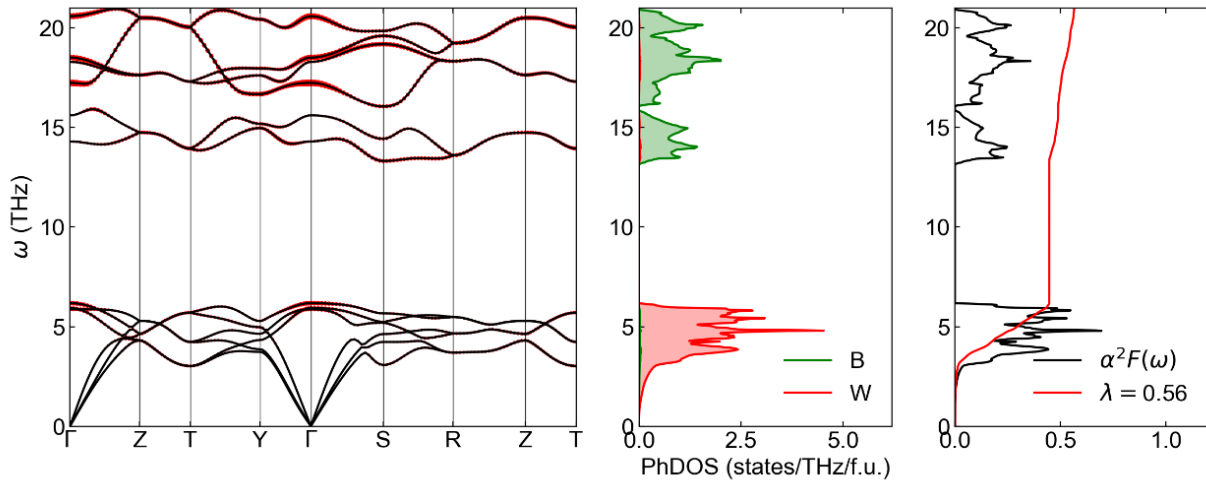


Fig. S14. Phonon dispersion, phonon density of state, and Eliashberg spectrum of WB. The red bands on the phonon dispersion indicate the strength of EPC.

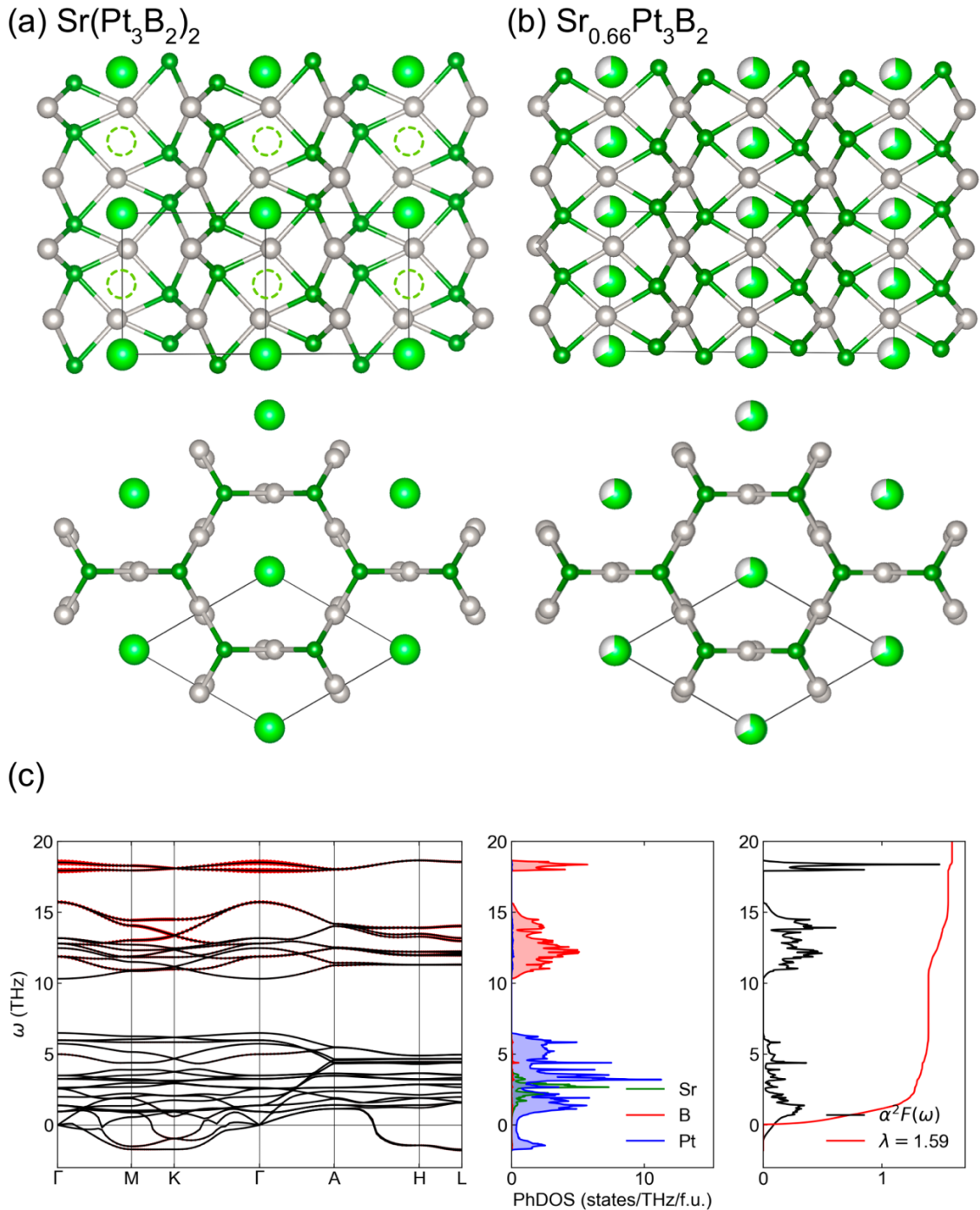


Fig. S15. (a) Structure model of $\text{Sr}(\text{Pt}_3\text{B}_2)_2$. (b) The partially occupied $\text{Sr}_{0.66}\text{Pt}_3\text{B}_2$ model from the experiment (Journal of the Less Common Metals, 1978, 62: 191-196). The upper and lower figures show the side and top views. The dashed circle in (a) shows the vacancy Sr sites compared to the experimental structure. (c) Phonon dispersion, phonon density of state, and Eliashberg spectrum of $\text{Sr}(\text{Pt}_3\text{B}_2)_2$. The red bands on the phonon dispersion indicate the strength of EPC.

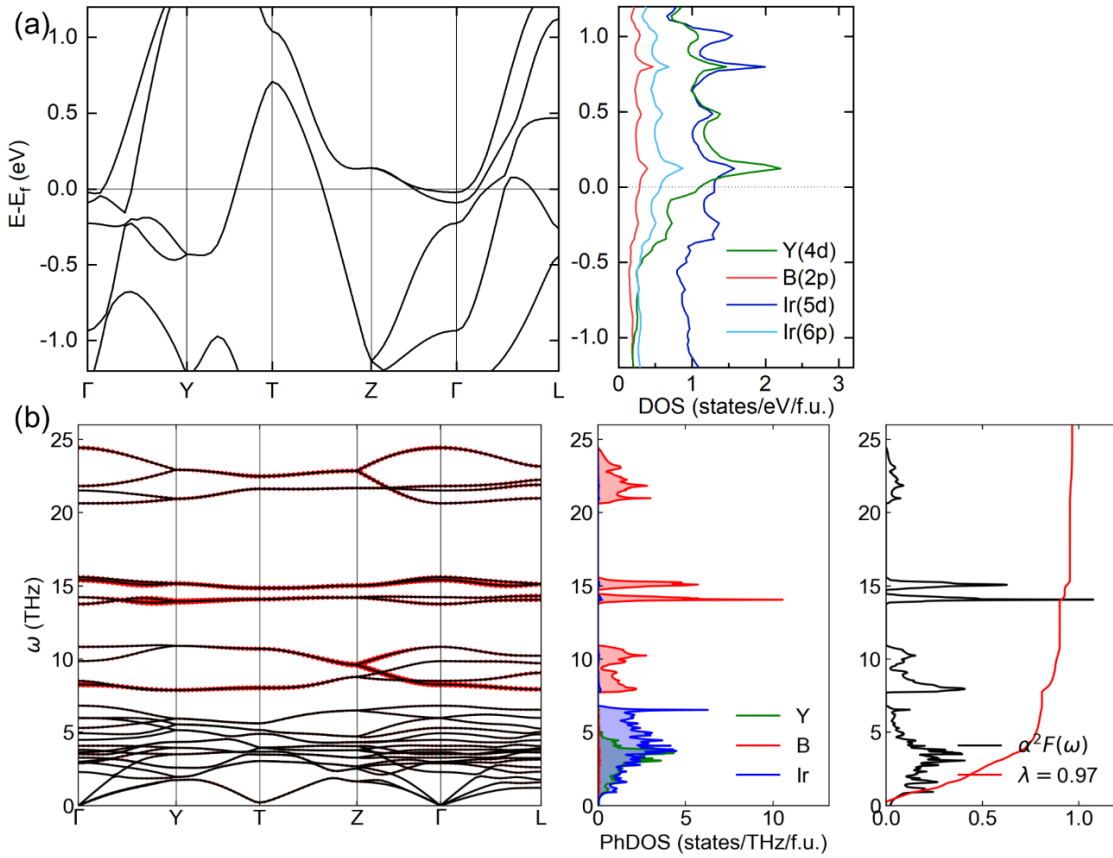


Fig. S16 (a) Band structure and projected density of states of YIr₂B₂. (b) Phonon dispersion, projected phonon density of state, and Eliashberg spectrum of YIr₂B₂. The red bands on the phonon dispersion indicate the strength of EPC.

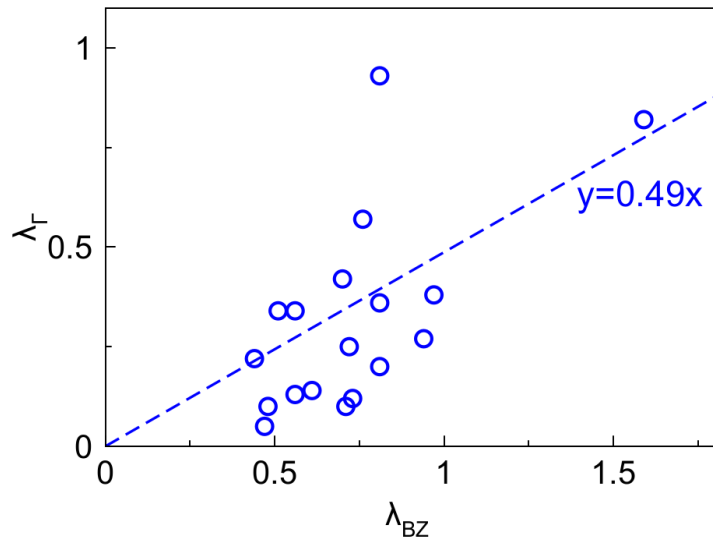


Fig. S17. A scatter plot of zone-center EPC strength λ_Γ versus the EPC constant λ_{BZ} from full Brillouin zone DFPT calculations. Dashed lines represent the corresponding linear relationships.

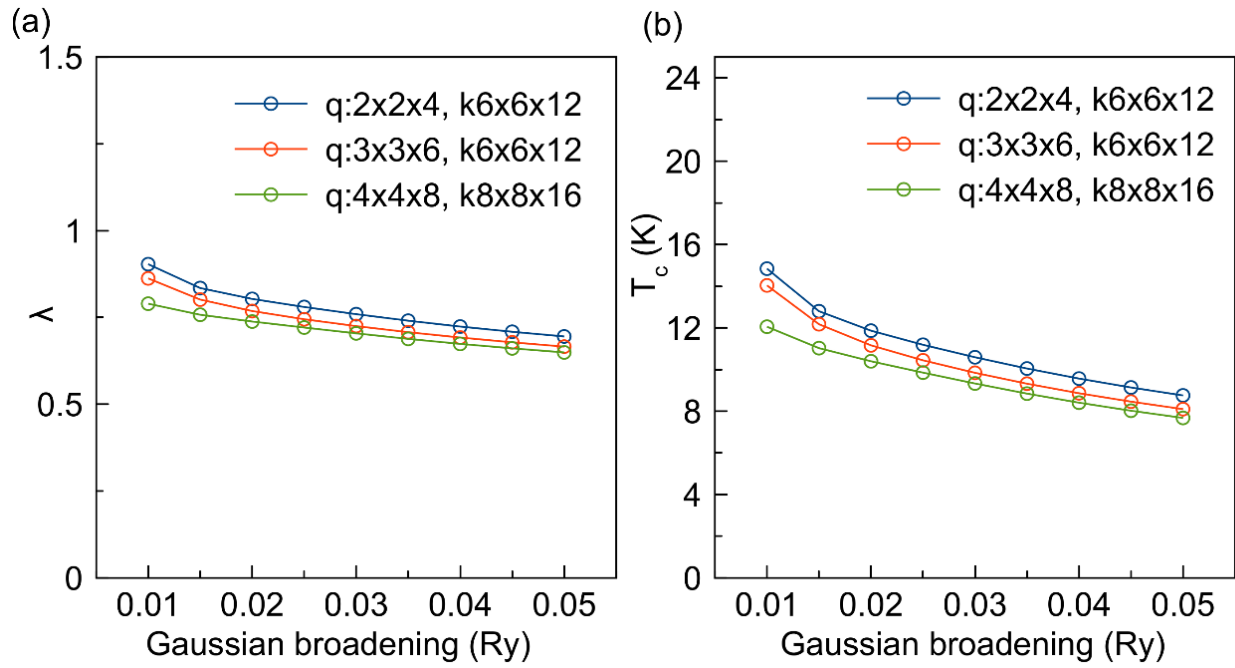


Fig. S18. (a) λ and (b) T_c dependence on the Gaussian broadening with different q- and k-meshes for TaMo₂B₂ system. “q:4×4×8, k:8×8×16” indicates a 4×4×8 q-mesh and 8×8×16 k-mesh in DFPT calculations, and a k-meshes of 16x16x32 for EPC matrix calculation.